

# X-ray Constraints on Accretion and Starburst Processes in Galactic Nuclei I. Spectral Results

A. Ptak<sup>1</sup>, P. Serlemitsos, T. Yaqoob<sup>2</sup>, R. Mushotzky  
*NASA GSFC, Code 662, Greenbelt, MD 20771*

## ABSTRACT

The results of the analysis of 0.4-10.0 keV *ASCA* spectral analysis of a sample of low-luminosity AGN (LLAGN; M51, NGC 3147, NGC 4258), low-ionization nuclear emission line regions (LINERs; NGC 3079, NGC 3310, NGC 3998, NGC 4579, NGC 4594) and starburst galaxies (M82, NGC 253, NGC 3628 and NGC 6946) are presented. In spite of the heterogeneous optical classifications of these galaxies, the X-ray spectra are fit well by a “canonical” model consisting of an optically-thin Raymond-Smith plasma “soft” component with  $T \sim 7 \times 10^6$  K and a “hard” component that can be modeled by either a power-law with a photon index  $\Gamma \sim 1.7$  or a thermal bremsstrahlung with  $T \sim 6 \times 10^7$  K. The soft component absorption is typically less than  $10^{21}$  cm<sup>-2</sup> while the hard component is typically absorbed by an additional column on the order of  $10^{22}$  cm<sup>-2</sup>. The soft-component 0.4-10 keV intrinsic luminosities tend to be on the order  $10^{39-40}$  ergs s<sup>-1</sup> while the hard-component luminosities tend to be on the order of  $10^{40-41}$  ergs s<sup>-1</sup>. The abundances inferred from the fits to the soft-component are significantly sub-solar. The Fe abundance can be measured independently of the other elemental abundances (dominated by  $\alpha$ -process elements) in M51, M82, NGC 253, and NGC 4258. In these galaxies the Fe abundance relative to  $\alpha$ -process elements is also (statistically) significantly sub-solar. There is some indication (at a low-statistical significance) that the abundance

---

<sup>1</sup>Present address: Carnegie Mellon University, Department of Physics, Pittsburgh, PA 15213

<sup>2</sup>Also with USRA

properties starburst emission from starburst galaxies differs from the starburst emission from low-luminosity AGN. However, these results on abundances are model-dependent. Significant Fe-K line emission is observed in M51, M82, NGC 3147, NGC 4258 and NGC 4579. An analysis of the short-term variability properties was given in (Ptak et al. 1998a) and detailed interpretation of these results will be given in Paper II (Ptak et al. 1998b).

*Subject headings:* galaxies: abundances — galaxies:active — galaxies: ISM — galaxies: starburst — accretion — ISM: abundances — ISM: kinematics and dynamics — X-rays: galaxies — X-rays: ISM

## 1. Introduction

Observations by the imaging X-ray satellite *Einstein* showed that “normal” spiral galaxies tend to have X-ray luminosities on the order of  $10^{38-41}$  ergs  $s^{-1}$  and spectra consistent with the superposition of (typical) X-ray binary spectra (see Fabbiano 1989 for a review). In some cases, extended X-ray emission and multiple extra-nuclear point-sources were detected (c.f., M82 in Watson, Stanger, & Griffiths 1984 and Fabbiano 1988; NGC 253 in Fabbiano & Trinchieri 1984 and Fabbiano 1988; M51 in Palumbo et al. 1985). However, the high spectral resolution of *ASCA* (see Tanaka, Inoue, & Holt 1994) is necessary to provide further insight into the nature of the X-ray emission. Early results from the *ROSAT* All-Sky Survey (Boller et al. 1992) found that some non-AGN spiral galaxies may be as bright as  $L_{0.1-2.2 \text{ keV}} \sim 10^{42}$  ergs  $s^{-1}$  and suggested that these high X-ray luminosities may be due to very powerful starburst activity. An optical follow-up to this study showed that RASS galaxies with  $L_{0.1-2.2 \text{ keV}} \gtrsim 10^{42}$  ergs  $s^{-1}$  tended to be low-luminosity AGN (LLAGN; Moran, Halpern, & Helfand 1994; Moran 1996) and the *ASCA* spectra of one of these galaxies, NGC 3147, revealed X-ray properties consistent with Seyfert 2 galaxies (see Ptak et al. 1996).

In this paper we present the results of *ASCA* spectral analysis of a sample of “low-activity” galaxies consisting of LLAGN, LINERs, and starbursts. This sample is listed in Table 1, which also lists the Galactic column densities and the distances to each galaxy, and Table 2 gives a log of the *ASCA* observations. The sample is based on galaxies with public and proprietary *ASCA* data available to us as of the summer of 1996 and is not

complete in any sense. However, this study will hopefully give some insight into the nature of the X-ray emission beyond that which might be expected from “normal” galaxies. In cases where there is strong evidence for the presence of a low-luminosity AGN, this analysis will demonstrate the extent to which the X-ray properties of these galaxies are simply an extension of the X-ray properties of normal Seyferts to lower luminosities. As discussed in Ptak et al. (1998a), the variability behavior of these low-activity galaxies differs significantly from the trends of normal AGN. Specifically, much less short-term variability is observed than expected. This suggests a different mode of accretion, and this may also have spectral implications as well (see Paper II for a full discussion).

*ROSAT* PSPC spectra were also analyzed along with the *ASCA* data, with emphasis on improving the determination of the absorbing column along the line of sight. While the spectral resolution of the PSPC is relatively poor, the sensitivity of *ROSAT* to photons in the 0.1-0.3 keV range makes it much more sensitive to columns on the order of  $10^{19-20}$   $\text{cm}^{-2}$  than *ASCA*. A log of the PSPC observations discussed in this paper is given in Table 3.

## 2. Summary of Previous X-ray Observations

Dahlem, Weaver, & Heckman (1998; hereafter DWH) discuss spatial analysis of the *ROSAT* PSPC and HRI data and spectral analysis of the *ASCA* and *ROSAT* pspc data for a sample of starburst galaxies, including NGC 253, NGC 3079, NGC 3628, and M82 which are discussed here. DWH found evidence for three-component fits to the *ASCA* and *ROSAT* PSPC spectra from these galax-

TABLE 1

Galaxy	R.A., Decl. (J2000)	Type*	$N_{H,Gal.}$ ( $10^{20} \text{ cm}^{-2}$ )	Distance (Mpc)	ASCA PSF** (kpc)
NGC 253	00h47'33.1, -25d7'18	H	1.3 <sup>a</sup>	2.5 <sup>b</sup>	2.2
NGC 3079	10 01 57.8, 55 40 47	S2	0.8 <sup>a</sup>	28.8 <sup>c</sup>	25
NGC 3147	10 16 53.2, 73 24 04	S2	2.5 <sup>d</sup>	56.4 <sup>c</sup>	49
NGC 3310	10 38 45.9, 53 30 12	H	1.4 <sup>j</sup>	19.4 <sup>c</sup>	17
NGC 3628	11 20 17.0, 13 35 20	T2	2.2 <sup>j</sup>	14.9 <sup>c</sup>	13
NGC 3998	11 57 56.1, 55 27 13	L1.9	1.0 <sup>j</sup>	24.3 <sup>f</sup>	21
NGC 4258	12 18 57.5, 47 18 14	S1.9	1.2 <sup>j</sup>	10.2 <sup>g</sup>	8.9
NGC 4579	12 37 43.5, 11 49 05	S1.9/L1.9	3.1 <sup>j</sup>	36.1 <sup>c</sup>	32
NGC 4594	12 39 58.8, -11 37 28	L2	3.8 <sup>j</sup>	22.6 <sup>c</sup>	20
NGC 6946	20 34 52.3, 60 09 14	H	20-50 <sup>a,h</sup>	8.3 <sup>g</sup>	7.2
M51	13 29 52.4, 47 11 54	H	1.3 <sup>a</sup>	14.0 <sup>c</sup>	12
M82	09 55 52.2, 69 40 47	H	4.3 <sup>a</sup>	3.6 <sup>i</sup>	3.1

REFERENCES.—a) Fabbiano et al. (1992), b) de Vaucouleurs (1963), c) Soifer et al. (1987), Stark et al (1992), e) Hartmann & Burton (1995), f) de Vaucouleurs et al. (1991), g) Tully (1988), h) Burstein & Heiles (1984), i) Freedman et al. (1994), j) Murphy et al. (1996)

\*Optical classification given in Ho et al. (1997a) (the optical classification for NGC 253 is from NED). H=HII region/starburst galaxy, T = transition starburst/LINER galaxy, L = LINER galaxy, S = Seyfert galaxy.

\*\*Distance corresponding to  $3' \sim$  the *ASCA* half-power diameter.

TABLE 2  
*ASCA* OBSERVATION LOG

Galaxy	Number <sup>a</sup>	Date	CCD Mode <sup>b</sup>	Exposure (ks) <sup>c</sup>	SIS Region Size
NGC 253	60038000	Jun. 12, 1993	4	33.5, 33.6, 36.2, 36.2	6
NGC 3079	60000000	May 9, 1993	1	41.0, 41.1, 40.8, 40.2	4
NGC 3147	60040000	Sep.29, 1993	4	22.4, 23.0, 38.7, 39.0	4
NGC 3310	61013000	Apr. 17, 1994	1	17.7, 15.3, 17.9, 17.9	4
NGC 3310	61013010	Nov. 13, 1994	2	10.2, 9.9, 10.3, 10.3	4
NGC 3310	61013020	Apr. 11, 1995	1	10.7, 10.6, 11.3, 11.3	4
NGC 3628	61015000	Dec. 12, 1993	2	17.5, 20.2, 23.9, 23.9	3
NGC 3998	71048000	May 10, 1994	2	40.8, 38.6, 40.0, 39.9	4
NGC 4258	60018000	May 15, 1993	4	33.0, 34.1, 40.1, 40.1	6
NGC 4579	73063000	Jun. 25, 1995	2	36.0, 34.0, 34.6, 34.6	4
NGC 4594	61014000	Jan. 20, 1994	2	19.6, 18.2, 20.1, 20.1	4
NGC 6946	60039000	May 31, 1993	4	20.2, 20.5, 27.0, 27.0	4
M51	60017000	May 11, 1993	4	32.4, 33.1, 38.1, 38.1	6
M51	15020100	May 4, 1994	4	16.9, 11.2, 42.5, 42.5	6
M82	60001000	Apr. 19, 1993	4	18.1, 18.2, 27.8, 27.3	6

<sup>a</sup>Reference number for this observation in the *ASCA* archival database

<sup>b</sup>Number of active CCDs

<sup>c</sup>Exposure times for SIS0, SIS1, GIS2, and GIS3

TABLE 3  
*ROSAT* OBSERVATION LOG

Galaxy	Number <sup>a</sup>	Dates	Exposure (ks)
NGC 253	rp600087a00	Dec. 25-31, 1991	11.6
NGC 253	rp600087a01	Jun. 3-5, 1992	11.2
NGC 3079	rp700319n00	Nov. 14-15, 1991	16.3
NGC 3147	wp600589n00	Oct. 16-22, 1991	8.5
NGC 3310	rp600156n00	Nov. 17-18, 1991	8.0
NGC 3628	rp700010n00	Nov. 23-6, 1991	13.9
NGC 3998	rp700055	May 22-24, 1991	55.9
NGC 4258	rp600186n00	May 9, 1992	5.3
NGC 4258	wp600546n00	Nov. 11-15, 1993	25.4
NGC 4579	rp700056n00	Dec. 15-16, 1991	8.9
NGC 4594	rp600258n00	Jul. 15-19, 1992	10.6
NGC 6946	rp600272n00	Jun. 16-21, 1992	35.6
M51	rp600158n00	Nov. 28 - Dec. 13, 1991	22.2
M82	rp600110a00	Mar. 27-29, 1991	10.6
M82	rp600110a01	Oct. 15-16, 1991	10.7
M82	wp600576n00	Sep. 29 - Oct. 3, 1993	17.0

<sup>a</sup>Reference number for this observation in the *ROSAT* archival database

ies, which are discussed in §6.7.

## 2.1. NGC 253

NGC 253 was observed by pointed observations with both the *Einstein* HRI (Fabbiano & Trinchieri 1984) and IPC (Fabbiano 1988). The HRI observation shows that there were  $\sim 8$  extra-nuclear X-ray sources, with X-ray luminosities in the range of  $1-5 \times 10^{38}$  ergs  $s^{-1}$ . The nucleus is extended over  $\sim 12''$ , occupying a similar region as the nuclear radio and IR emission but not elongated along the major axis as these components are. The estimated luminosity of the nucleus was  $\sim 3 \times 10^{39}$  ergs  $s^{-1}$ . Of course, these luminosity estimates are sensitive to assumptions concerning the source spectra, particularly the assumed amount of absorption. The IPC observation, which is more appropriate for studying diffuse flux, showed that the X-ray radial profile is steeper than the optical (blue) profile along the major axis and agrees better with the radio profile. The X-ray emission along the minor axis, associated with superwind outflow, extends to  $\sim 9$  kpc, further than the optical or radio flux. The X-ray radial profile along the minor axis was consistent with a density distribution  $\rho \sim r^{-2}$  as would be expected for a freely-expanding wind. The energy resolution of the IPC was rather poor ( $\Delta E/E \sim 100\%$ ) but showed that the spectrum of NGC 253 is consistent with a  $\sim 5$  keV bremsstrahlung model with absorption on the order of the Galactic column density,  $\sim 2 \times 10^{20}$   $cm^{-2}$ . Fabbiano (1988) estimates the halo gas density, mass and radiative lifetime at  $1.7 \times 10^{-3} f^{-1/2}$   $cm^{-3}$ ,  $2.2 \times 10^7 f^{1/2} M_{\odot}$ , and  $2.1 \times 10^9 f^{1/2}$  yr, where  $f$  is the volume filling factor (see Paper II for a detailed discussion).

Ohashi et al. (1990) found that *Ginga* detected NGC 253 with a 2-10 keV flux of  $\sim 7.0 \times 10^{-12}$  ergs  $cm^{-2}$   $s^{-1}$  ( $L_{2-10 \text{ keV}} \sim 9.7 \times 10^{39}$  ergs  $s^{-1}$ ). Bhattacharya et al. (1994) report the detection of NGC 253 by the *Compton Gamma-Ray Observatory (CGRO)* at a flux level about an order of magnitude above the extrapolated *Ginga* flux. This detection was interpreted by Goldshmidt & Raphaeli (1995) as inverse-Compton scattered IR flux and microwave cosmic background flux. The *BBXRT* 0.3-10.0 keV spectrum of NGC 253 was fit well with a double Raymond-Smith plasma model with temperatures of  $\sim 0.6$  and 6 keV (Petre 1993). *ROSAT* PSPC data showed that the 0.1-0.4 keV flux is most prominent in the halo while the 0.5-2.4 keV flux is most prominent in the disk, suggesting that the halo emission is significantly cooler than the disk emission (Pietsch 1995). Read, Ponman, & Strickland (1997) found 7 sources in addition to the *Einstein* sources. The PSPC data show that several of the sources are hard ( $kT > \text{several keV}$ ) and are therefore likely to be X-ray binaries rather than supernova remnants. Read, Ponman, & Strickland (1997) also found that  $\sim 74\%$  of the flux in the PSPC bandpass appears to be “diffuse”, although the high value of  $\chi^2_{\nu}$  for a thermal fit to the diffuse component suggests that a significant fraction of the diffuse flux may be due to unresolved point sources. Analysis of the *ASCA* data was presented in Ptak et al. (1997) and is discussed in the remainder of this paper.

## 2.2. NGC 3079

NGC 3079 was detected by the *Einstein* IPC at the 3.2s level (Fabbiano, Feigelson & Zamorani 1982), with an estimated flux of  $3.7 \times 10^{-13}$  ergs  $cm^{-2}$   $s^{-1}$ . Reichert,

Mushotzky & Filippenko (1994) found that the *ROSAT* PSPC data from NGC 3079 is dominated by a nuclear point source but that X-ray emission is detected up to 2.5' from the nucleus. Above 0.5 keV the X-ray emission is slightly elongated along the (optical and radio) major axis. Below 0.5 keV there is a “soft patch” 1-2' northeast of the nucleus. The best-fitting spectral model for the galaxy was a Raymond-Smith plasma plus power-law model with  $kT \sim 0.4$  keV and a photon index  $\Gamma$  of  $\sim 1.6$ . Read, Ponman, & Strickland (1997) found that  $\sim 69\%$  of the flux from NGC 3079 is diffuse in the *ROSAT* bandpass. The diffuse PSPC flux is fit well by a thermal model (with  $kT \sim 0.5$  keV and abundances  $\sim 0.03 \times$  solar).

### 2.3. NGC 3147

NGC 3147 was not detected significantly by *Einstein*, although emission at the  $3\sigma$  level was detected by *HEAO-I* in the vicinity of NGC 3147 (Rephaeli, Gruber, & Persic 1995). Analysis of the *ASCA* data was presented in Ptak et al. (1996). The authors found that the spectrum appeared to be absorbed by a column  $< 10^{21}$  cm $^{-2}$ , which indicated that either the nucleus was truly unobscured, or that the X-ray flux was scattered into the line of sight. In addition, the detection of a large equivalent width Fe line and the optical classification of the source as a Seyfert 2 strongly indicates that the X-ray flux from NGC 3147 is indeed scattered into the line of sight.

### 2.4. NGC 3628

Although NGC 3628 is a starburst galaxy, it has exhibited dramatic X-ray variability. The 0.1-2.0 keV X-ray flux detected by the *Einstein* IPC  $\sim 8 \times 10^{-13}$  ergs cm $^{-2}$  s $^{-1}$  in 1979 and the X-ray flux in this bandpass de-

tected by the *ROSAT* PSPC in 1991 was at approximately the same level, but the *ASCA* flux was at a level of  $3 \times 10^{-13}$  ergs cm $^{-2}$  s $^{-1}$  in 1993 and a HRI observation in 1994 resulted in an upper limit of  $\sim 0.5 \times 10^{-13}$  ergs cm $^{-2}$  s $^{-1}$  (Dahlem, Heckman, & Fabbiano 1995). (Note that the *Einstein* and *ASCA* flux estimates in this bandpass require some extrapolation since their sensitivity only extends down to  $\sim 0.4$  keV.) This variability obviously shows that the nucleus is dominated by a point-source, most likely a micro-AGN or an X-ray binary. The X-ray luminosity of  $\sim 1 \times 10^{40}$  ergs s $^{-1}$ , if sub-Eddington, implies that the mass of any accreting object would have to be  $> 75M_{\odot}$ . Diffuse X-ray emission associated with the halo of NGC 3628 is discussed in Dahlem et al. (1996) and is evidence for a superwind similar to the ones observed in M82 and NGC 253. The *ASCA* spectrum was observed to be very flat, leading Yaqoob et al. (1995) to suggest that if a large population of galaxies with a similar spectrum is detected, then these galaxies may contribute significantly to the X-ray background.

### 3. NGC 3310

NGC 3310 was detected by *Einstein* with a 0.5-4.5 keV flux of  $1.1 \times 10^{-12}$  ergs cm $^{-2}$  s $^{-1}$  and luminosity of  $4.9 \times 10^{41}$  ergs s $^{-1}$  (Fabbiano et al. 1992). A detailed analysis of the *ASCA* and *ROSAT* data of NGC 3310 in Zezas, Georgantopoulos, & Ward (1998) showed that the soft emission is extended over  $\sim 3$  kpc and that, as with other starbursts such as NGC 253 and M82, the broadband (0.1-10.0 keV) X-ray spectrum consists of at least two components: a  $kT \sim 0.8$  keV soft component and a hard component fit well with a power-law with a photon index of  $\sim 1.4$  or a thermal component with  $kT \sim 15$  keV.



## 4. NGC 3998

Awaki et al. (1991) found that the Ginga flux measured for NGC 3998 was about 3 times larger (extrapolated) than the 0.4-3.5 keV *Einstein* flux ( $5.0 \times 10^{-12}$  ergs cm $^{-2}$  s $^{-1}$ ) given in Dressel & Wilson (1985). A thermal model fit to NGC 3998's 2-20 keV spectrum could be rejected while a power-law model with a slope of  $\sim 2$  provided a good fit. Reichert, Mushotzky & Filippenko (1994) found that the best-fit to the *ROSAT* PSPC spectrum for NGC 3998 was a broken power-law with slopes of 1.3 and 2.1 and a break energy of  $\sim 0.8$  keV. No extended emission was found in the PSPC data.

### 4.1. NGC 4258

*Einstein* detected NGC 4258 with a luminosity of  $5.9 \times 10^{39}$  ergs s $^{-1}$  (Fabbiano et al. 1992). A *ROSAT* PSPC observation showed that the extranuclear X-ray flux in NGC 4258 is dominated by jets (Cecil, Wilson & De Pree 1995), and that the X-ray emission is due to shock-heating along the jet. Makishima et al. (1994) found that *ASCA*'s 0.4-10.0 keV spectra of NGC 4258 exhibited at least two components: hot gas associated with the jet and a highly-absorbed power-law associated with a Seyfert 2 nucleus. NGC 4258 is one of the few galaxies with a well-determined blackhole mass (Greenhill, et al. 1995), allowing its Eddington luminosity to be determined. Lasota et al. (1995) modeled the low luminosity of the AGN in NGC 4258 with an advection-dominated accretion flow, however Neufeld & Maloney (1995) modeled the accretion flow in a "normal," optically-thick (albeit warped) accretion disk.

### 4.2. NGC 4579

NGC 4579 was detected by *Einstein* with a 0.5-4.5 keV luminosity of  $\sim 4.7 \times 10^{40}$  ergs s $^{-1}$  (Green, Anderson, & Ward 1992). Reichert et al. (1994) found that the *ROSAT* PSPC flux is unresolved with an upper limit on the source extent of  $\sim 5''$ . The PSPC spectrum is best fit with a Raymond-Smith plus power-law model with kT  $\sim 0.5$  keV and a photon index  $\sim 1.9$ . A detailed analysis of the *ASCA* data presented in this paper is given in Terashima et al. (1998b).

### 4.3. NGC 4594

An *Einstein* IPC observation of NGC 4594 detected an 0.5-4.5 keV X-ray luminosity of  $\sim 8.7 \times 10^{40}$  ergs s $^{-1}$  (Green, Anderson, & Ward 1992). An analysis of *ROSAT* PSPC and HRI data by Fabbiano & Juda (1997) found that the nucleus is dominated by a point-like source with a 0.1-2.4 keV luminosity of  $\sim 3.5 \times 10^{40}$  ergs s $^{-1}$ , most likely due to a low-luminosity AGN. Given the high black-hole mass estimated by Kormendy & Richstone (1995) of  $\sim 5 \times 10^8 M_{\odot}$ , this AGN emission appears to be highly sub-Eddington ( $L_{Edd} \sim 6 \times 10^{46}$  ergs s $^{-1}$ ). There are 3 non-nuclear point-like sources with a (total)  $L_X \sim 2.1 \times 10^{40}$  ergs s $^{-1}$  and unresolved emission with  $L_X \sim 3 \times 10^{40}$  ergs s $^{-1}$  that may be due hot ISM or unresolved point-sources (such as X-ray binaries).

### 4.4. NGC 6946

The *Einstein* IPC detected two sources in NGC 6946, with a composite spectrum consistent with a thermal model with kT  $\sim 0.8$  keV (Fabbiano & Trinchieri 1987). A *ROSAT* PSPC observation resolved the X-ray emission from NGC 6946 into 8 sources, 3

of which constitute the IPC nuclear source (Schlegel 1994b). The brightest source is not the nucleus but rather a bright source  $\sim 2'$  to the north of the nucleus with  $L_X \sim 3 \times 10^{39}$  ergs  $s^{-1}$  that is interpreted as being a bright supernova remnant (Schlegel 1994a). The remaining sources each have a luminosity of  $\sim 10^{38}$  ergs  $s^{-1}$  and diffuse flux that traces the spiral-arm structure is detected with a total luminosity of  $\sim 10^{39}$  ergs  $s^{-1}$ . The diffuse emission is more consistent with hot ISM than unresolved point sources. The point sources are consistent with individual X-ray binaries or supernovae.

#### 4.5. M51

The *Einstein* HRI observation of M51 detected 3 unresolved sources in addition to nuclear and diffuse emission associated with M51 and M51's companion, NGC 5195 (Palumbo et al. 1985). Palumbo et al. found that the point-sources had estimated X-ray luminosities on the order of  $\sim 10^{39}$  ergs  $s^{-1}$ . M51's nucleus is extended over a  $\sim 24''$  region, with a point-source contribution of less than 20% to the total luminosity of  $\sim 8 \times 10^{39}$  ergs  $s^{-1}$ . The X-ray radial profile followed the blue light radio profile more closely than the spiral arm structure, indicating that a large fraction of the X-ray flux is due to disk population sources (i.e., X-ray binaries). A correlation between the X-ray profile and the non-thermal radio profile also suggests an association between X-ray emission and the relativistic electron population. A *Ginga* observation of M51 detected a 2-10 keV flux and luminosity of  $6.1 \times 10^{-12}$  ergs  $cm^{-2}$   $s^{-1}$  and  $6.7 \times 10^{40}$  ergs  $s^{-1}$  (Ohashi & Tsuru 1992) based on a power-law spectrum with a photon index of  $\sim 1.4$ . A *ROSAT* PSPC observation detected eight individual sources in addition

to nuclear and diffuse emission in M51, with luminosities in the range  $5 - 29 \times 10^{39}$  ergs  $s^{-1}$  (Marston et al. 1995). Of these sources, four appear to be associated with star-forming regions suggesting that the X-ray flux is due to young stellar processes, such as type-II supernovae, massive X-ray binaries, or possible "superbubbles" caused by multiple supernovae. A detailed analysis of the PV-phase *ASCA* is given in Terashima et al. (1998b) (note that this paper also includes the later AO-1 observation of M51).

#### 4.6. M82

M82 is one of the most studied galaxies at all wavelengths. Watson, Stanger & Griffiths (1984) found that the *Einstein* HRI data consists of up to 8 point-like sources with typical  $L_X \sim 5 - 9 \times 10^{38}$  ergs  $s^{-1}$ , some of which could be identified with nuclear HII regions or SN, comprising  $\sim 50\%$  of the nuclear flux. The nuclear region is extended over  $\sim 30''$  and has  $L_X \sim 7.4 \times 10^{39}$  ergs  $s^{-1}$ . Halo emission that is well-correlated with H $\alpha$  emission is detected out to a radius of  $\sim 3$  kpc. Fabbiano (1988) found that the *Einstein* IPC detected the X-ray halo out to a radius of  $\sim 9$  kpc with gas density, mass and radiative lifetime at  $2.1 \times 10^{-3} f^{-1/2}$   $cm^{-3}$ ,  $3.4 \times 10^7 f^{1/2}$   $M_{\odot}$ , and  $1.7 \times 10^9 f^{1/2}$  yr, where  $f$  is the volume filling factor (see Paper II). As with NGC 253, the X-ray surface brightness along the minor axis is consistent with a  $\rho \sim r^{-2}$  density distribution.

Schaaf et al. (1989) found that *EXOSAT* detected M82 with a 1.4-8.9 keV luminosity of  $3.2 \times 10^{40}$  ergs  $s^{-1}$  out to a radius of  $\sim 6$  kpc. The X-ray emission in this bandpass was fit well by a power-law model with photon index  $\sim 1.8$  or a thermal bremsstrahlung model with kT  $\sim 9$  keV. Schaaf et al. sug-

gest that most of the X-ray emission is non-thermal and is produced by inverse-Compton scattering of IR photons. Tsuru et al. (1990) reported a *Ginga* 2-10 keV luminosity for M82 of  $\sim 4 \times 10^{40}$  ergs s $^{-1}$  and found evidence for diffuse emission extended over  $\sim 100$  kpc. However, it must be kept in mind that *Ginga* is a non-imaging telescope so source confusion could be significant.

*ROSATHRI* observations showed that two of the X-ray sources in M82 are variable over time scales of years, and one of these, in close proximity to the nucleus, is variable on time scales of weeks (Collura et al. 1994; Ptak et al. 1997). A detailed analysis of the *ROSAT* HRI data by Bregman, Schulman, & Tomisaka (1995) showed that, in addition to the bright point-source mentioned above and two other sources with  $L_X \sim 10^{38}$  ergs s $^{-1}$ , the nuclear emission is consistent with an exponential distribution with an e-folding length of  $\sim 0.27$  kpc. X-ray emission is detected along the minor axis out to a distance of  $\sim 6$  kpc and has a surface brightness distribution beyond 1.6 kpc of the nucleus consistent with a power-law with an exponent of 2-3, again consistent with a freely-expanding wind. However, Strickland et al. (1997) found that the halo emission is more consistent with shock-heated clouds than a free-flowing wind on the basis of *ROSATHRI* and PSPC data. Moran & Lehnert (1997) found that the *ASCA* and *ROSAT* PSPC data from M82 are consistent with a power-law with slope of 1.7 and two thermal components with temperatures of  $\sim 0.3$  and 0.6 keV. Moran & Lehnert (1997) claim that the Raymond-Smith models for these thermal components do not adequately fit the data, but Ptak et al. (1997) and Tsuru et al. (1997) found that acceptable Raymond-Smith

fits can be found. Moran & Lehnert (1997) argue that the hard X-ray emission is likely to be due to inverse-Compton scattering of IR photons, while Ptak et al. (1997) found that the hard X-ray flux is most likely dominated by accreting sources, either blackhole candidate binaries or an AGN. Since these interpretations cannot be resolved spectrally (in the 2.0-10.0 keV bandpass), high-resolution imaging above 2 keV (as will be provided by *AXAF* and *XMM*) and/or detection of unambiguous variability above 2 keV will be required to distinguish among them.

## 5. Data Analysis Procedures

A detailed description of the data analysis procedures is given in Ptak (1997). Briefly, *ASCA* consists of two solid-state imaging spectrometers (SIS; hereafter S0 and S1) with an approximate bandpass of 0.4-10.0 keV and two gas imaging spectrometers (GIS; hereafter S2 and S3) with an approximate bandpass of 0.8-10.0 keV. Times of high background were excluded and hot pixels (in the SIS data) were removed. The sizes of the SIS source regions and the net exposure times are listed in Table 2. A 4' and 6' source region sizes would be appropriate SIS and GIS (respectively) sizes for a point source, however extended emission is clearly evident in some sources, requiring larger source regions for the SIS spectra (all of the sources are roughly point-like in the case of the GIS and so a 6' region was used). The background was estimated in two ways. First, background counts were extracted from an annulus exterior to the source region; hereafter backgrounds estimated in this way are referred to as "local". Second, background counts were summed from blank sky events lists in the same region as the source counts. The blank

sky events lists were obtained from archives at [legacy.gsfc.nasa.gov](http://legacy.gsfc.nasa.gov), and cleaning criteria consistent with the orbital parameters of each observation were applied. These backgrounds are referred to as blank sky backgrounds. The local backgrounds are most likely more robust since below  $\sim 1$  keV the SIS blank sky backgrounds are dominated by Galactic emission which varies as a function of Galactic position. The spectra have been binned to 20 counts per bin to allow the use of the  $\chi^2$  statistic. The data from the individual chips of each SIS were combined, however the spectra from each detector was fit separately (with the model parameters tied except for the overall normalization). The agreement in flux from the individual detectors is discussed in §6.3. Fits were attempted at first to just SIS spectra (which has higher spectral resolution than the GIS) and then to the SIS and GIS spectra. The best-fitting *ASCA* model was then also simultaneously fit to any available PSPC spectra (see §6.3). In all of the fits, all free parameters other than normalizations were considered to be “interesting” in determining 90% confidence intervals (see Cash 1979). Errors were computed automatically in the course of batch processing of the spectra although errors should be treated with caution for fits with  $\chi^2_\nu \gtrsim 1.5$ , where systematics may be important. Note that since these fits have on the order of hundreds of degrees of freedom, fits with  $\chi^2_\nu \sim 1.5$  can be rejected at a high level of confidence statistically, although again this does not incorporate any systematic error (the confidence probability with which the fits can be rejected is given in each table in parentheses with the  $\chi^2$  values).

## 6. Spectral Results

### 6.1. Single-Component Fits

The simplest model that can be fit to the spectra is a power-law ( $N(E) = e^{-N_H\sigma(E)} E^{-\Gamma}$ , where  $\sigma(E)$  is the neutral material cross section and  $N(E)$  gives photons  $\text{cm}^{-2} \text{s}^{-1} \text{keV}^{-1}$ ). The results of these fits are shown in Table 4. For eight of the galaxies the fits were “acceptable” (i.e., with  $\chi^2_\nu < 1.5$ ). Ratios of data to best-fitting model for the power-law fits are shown in Figure 1 where it can be seen that significant residuals remain. Significant line-like residuals are evident in the cases of M82 and NGC 253, while in lower signal-to-noise spectra residuals around 1 keV tend to be present. These residuals imply the presence of an optically-thin plasma. Accordingly, the Raymond-Smith plasma model was also fit to the spectra. In general there was no significant improvement in the fits, primarily because the temperature as determined by the centroid of the Fe-L complex centered around 1 keV tends to be less than 2 keV while the presence of significant emission above 2 keV implies a harder spectrum. In the cases of M51 and NGC 4258 it is clearly evident that more than one continuum component is required. An important point is the fact that while the spectra of some of the galaxies such as NGC 3147 and NGC 3998 are fit well by an unabsorbed power-law model, *none* of these galaxies has an X-ray spectrum consistent with *only an absorbed* (i.e.,  $N_H \gtrsim 10^{21} \text{cm}^{-2}$ ) power-law as might be expected from the hypothesis that the X-ray emission of these galaxies is due solely to the presence of an obscured AGN, without any other contribution to the X-ray flux.

### 6.2. Two-Component Fits

In order to simultaneously fit the line-like features and hard continuum, a two-

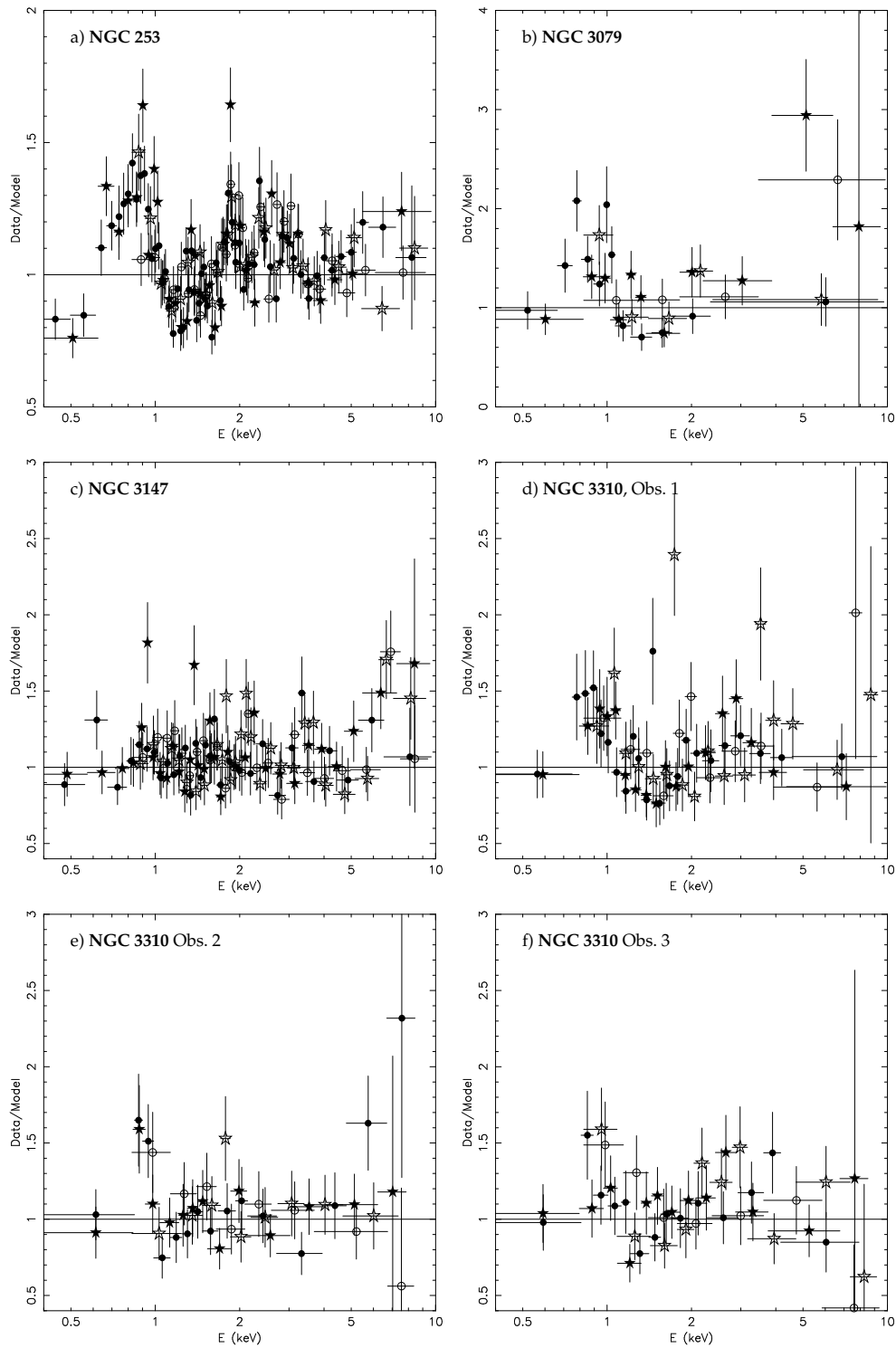


Fig. 1.— Ratio of data to power-law model (including neutral absorption) for each galaxy. Points show data from S0 (filled circles), S1 (filled stars), G2 (empty circles) and G3 (empty stars).

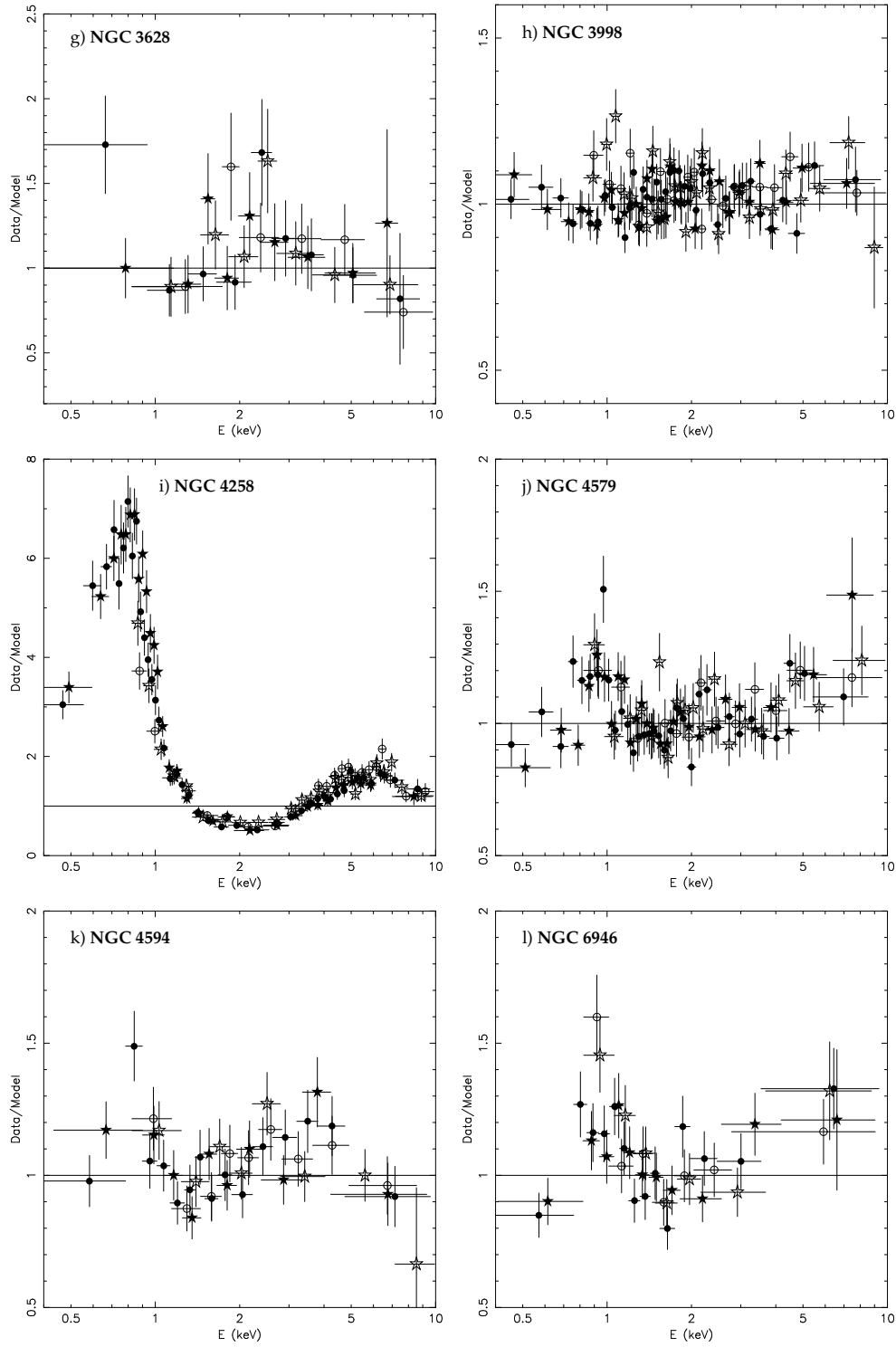


Fig. 1.— (cont.) Power-law Fit Data/Model Plots

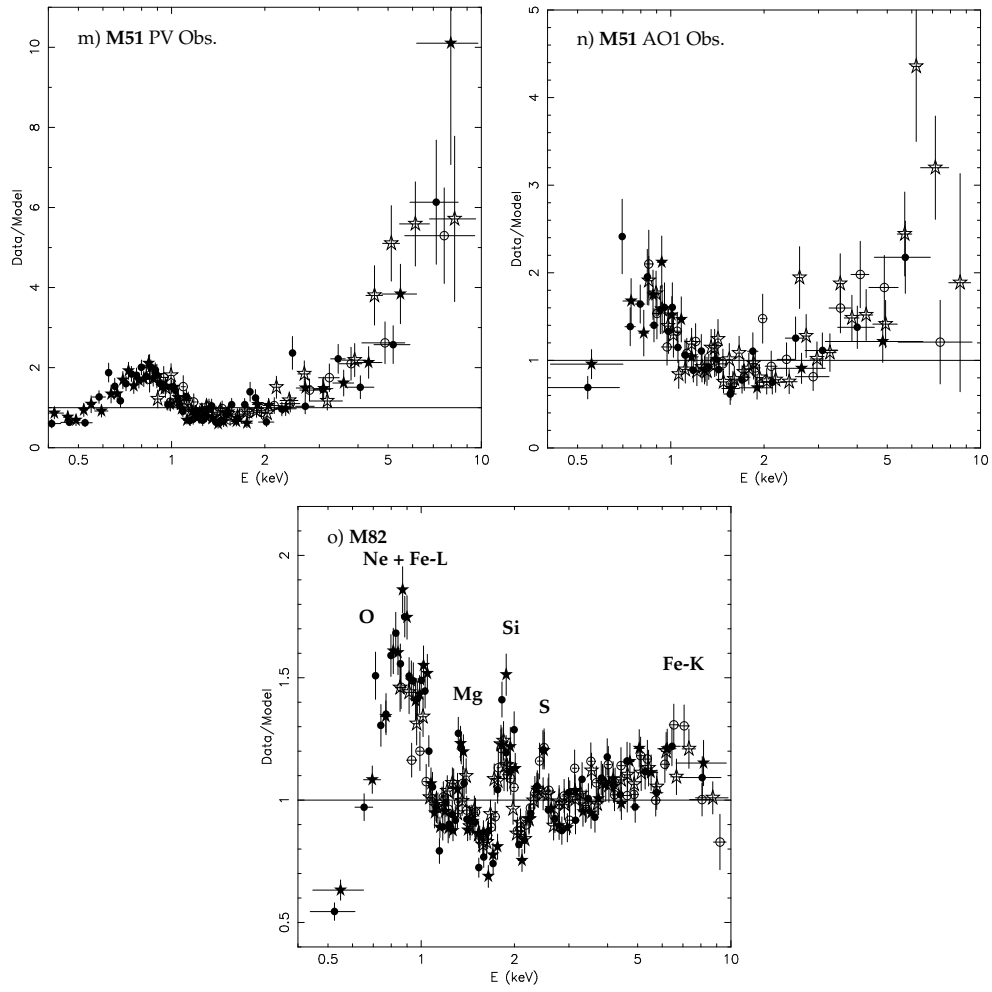


Fig. 1.— (cont.) Power-law Fit Data/Model Plots

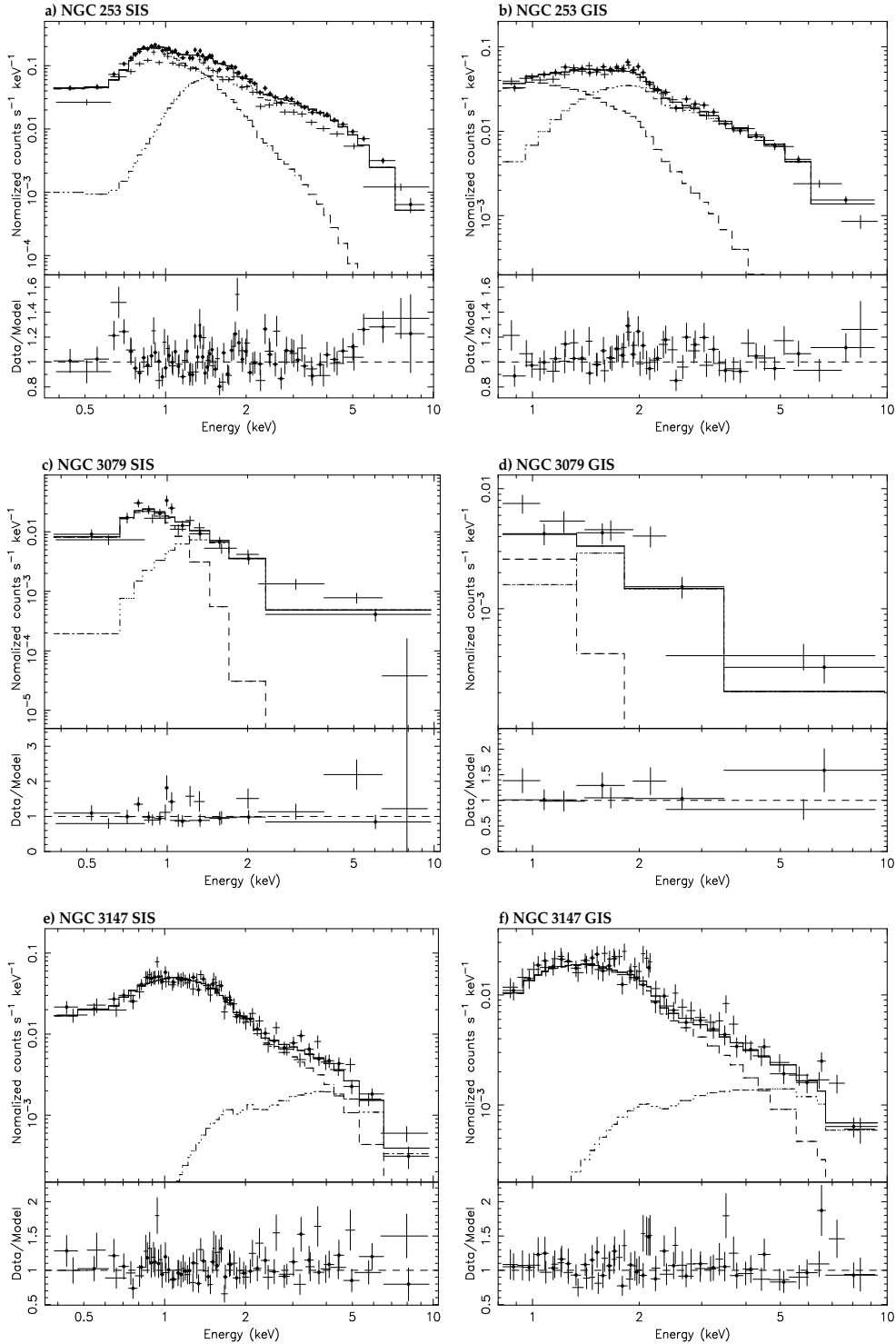


Fig. 2.— Best-fitting model, data, and data/model ratio for Raymond-Smith plus Power-law fits to the *ASCA* data. The best-fitting model is shown for the S0 data only, for clarity. The Raymond-Smith component is plotted with a dashed line and the power-law component is plotted with a dot-dashed line. The S0 and S2 points are marked (with filled circles) in the SIS and GIS plots, respectively.



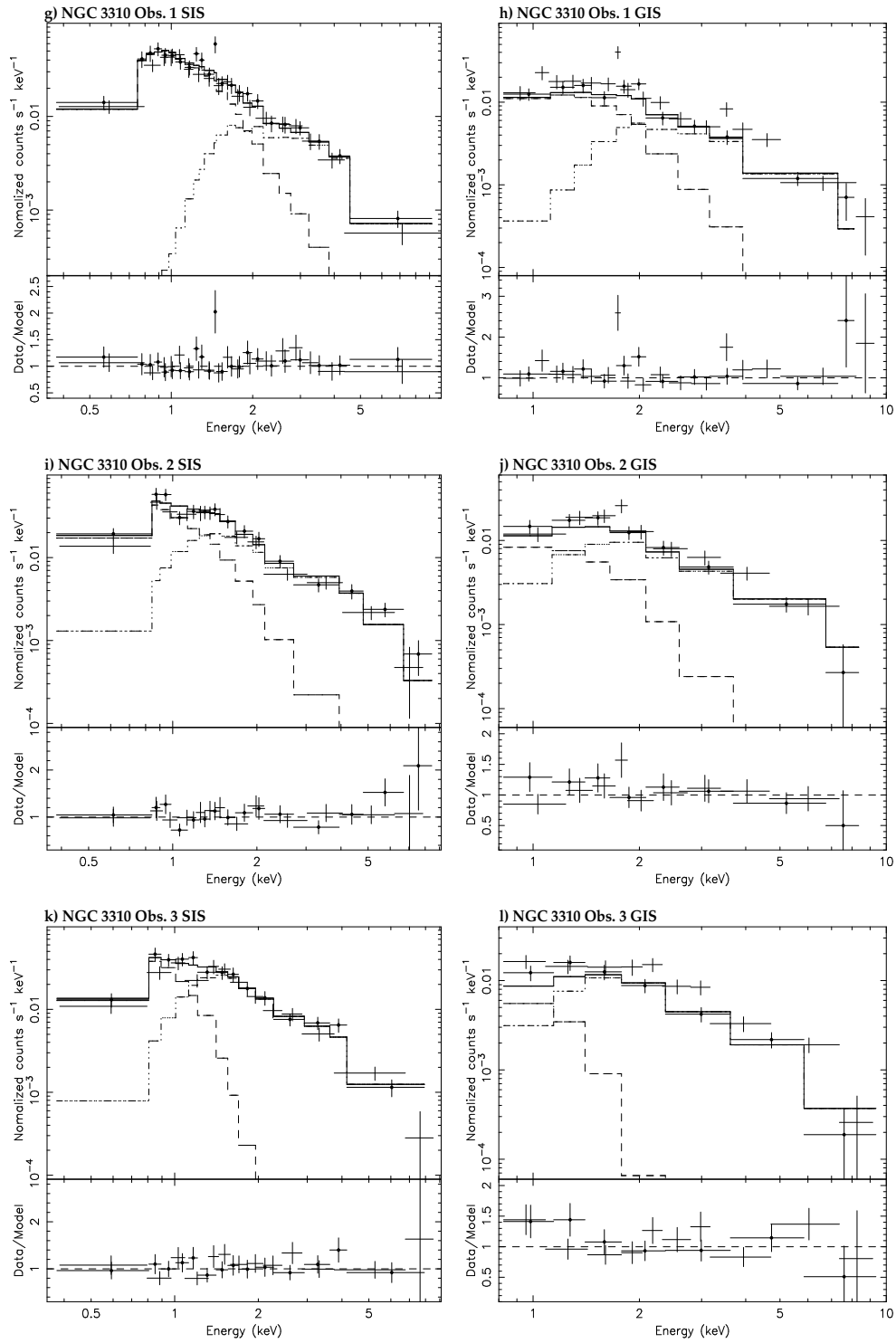


Fig. 2.— (cont.) Raymond-Smith plus Power-law Fits

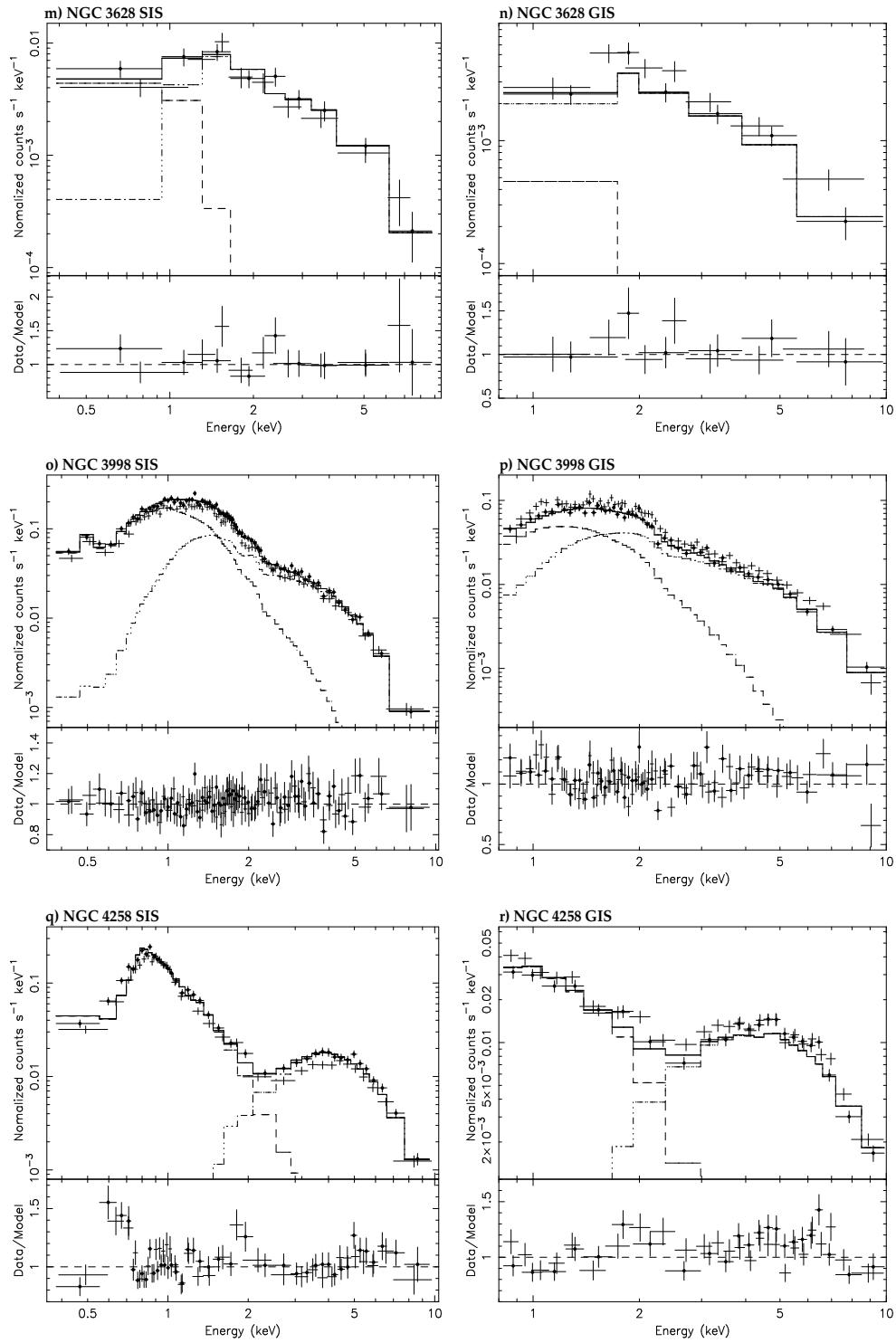


Fig. 2.— (cont.) Raymond-Smith plus Power-law Fits

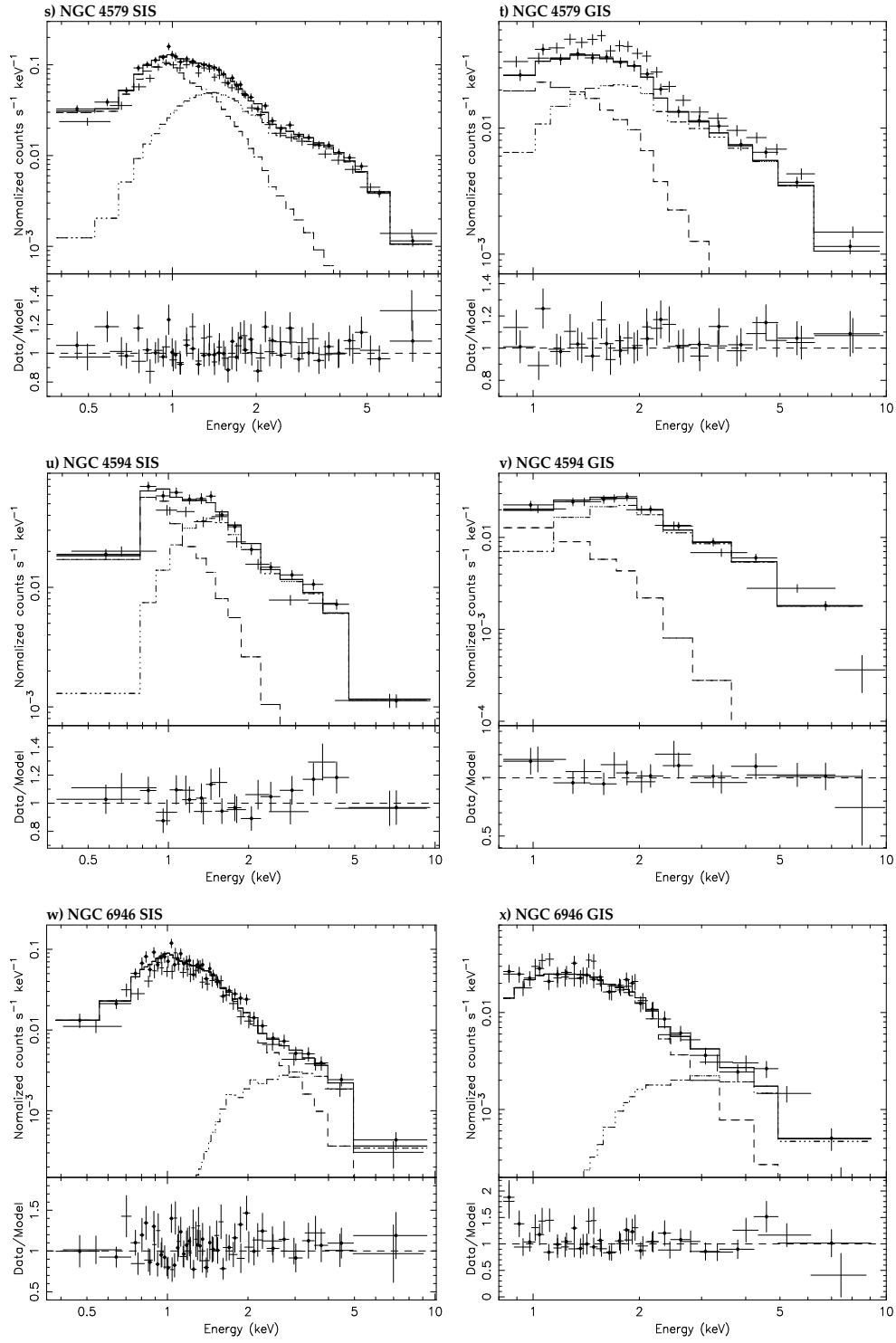


Fig. 2.— (cont.) Raymond-Smith plus Power-law Fits

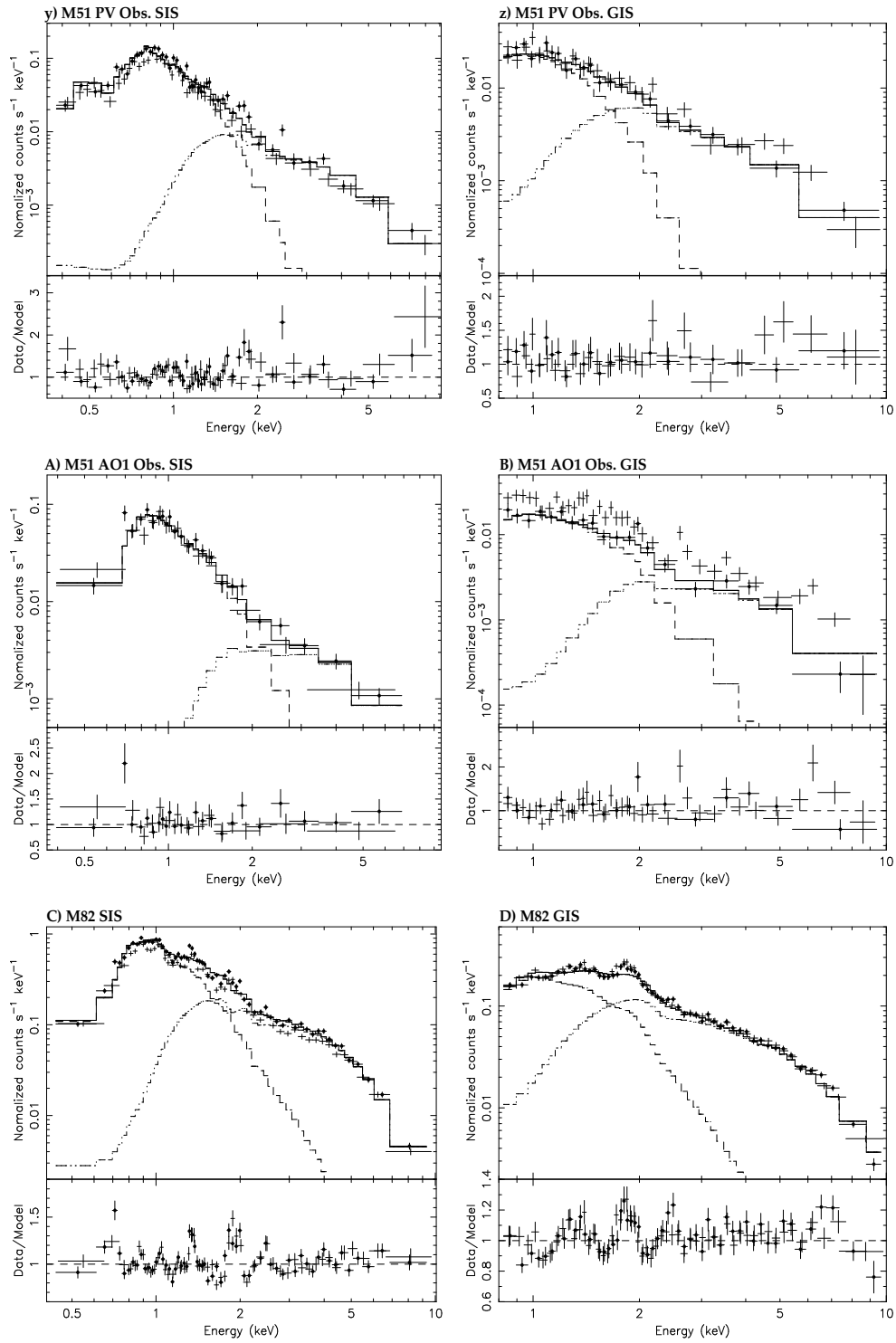


Fig. 2.— (cont.) Raymond-Smith plus Power-law Fits

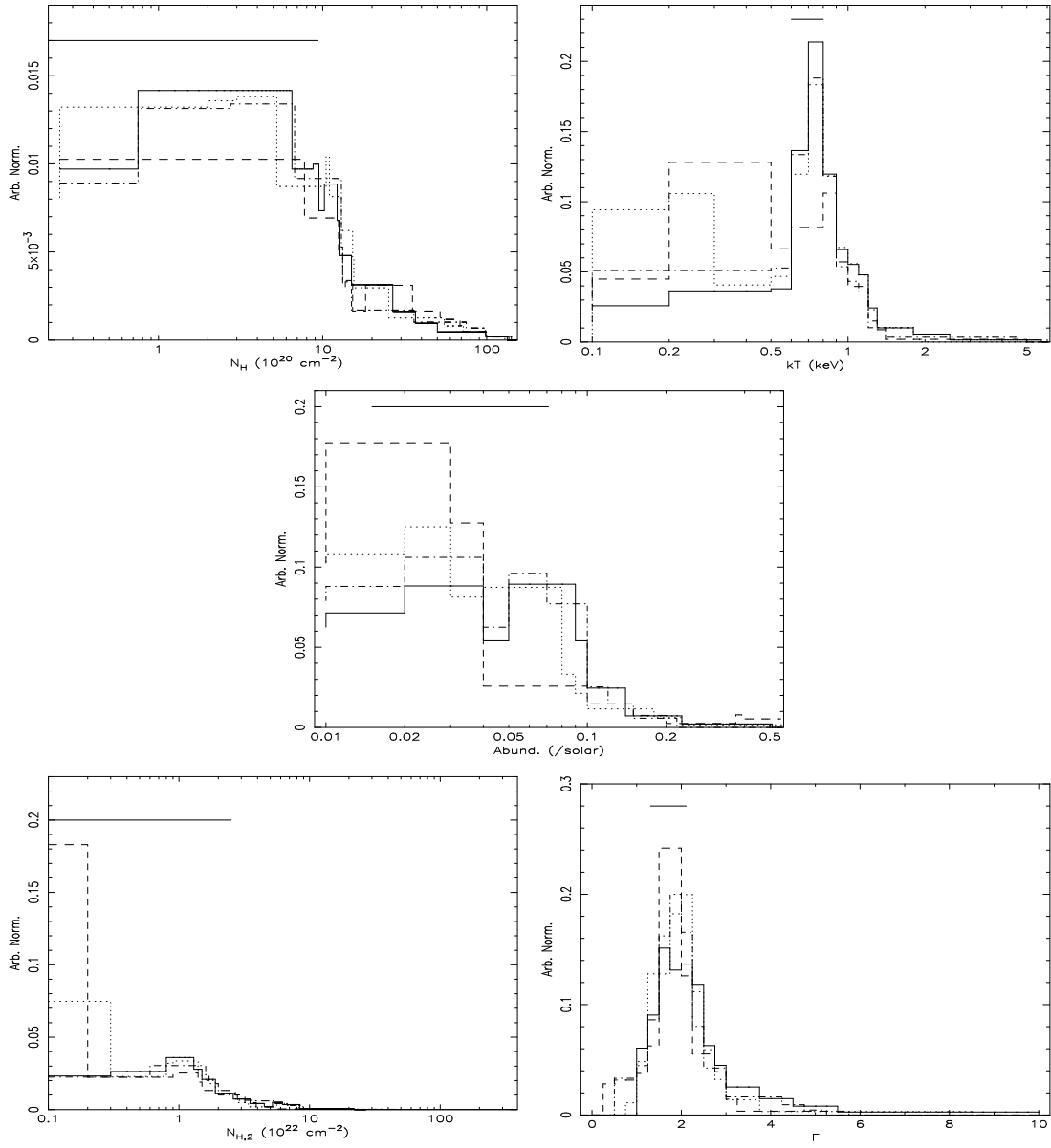


Fig. 3.— “Weighted” histograms of the best-fitting Raymond-Smith plus Power-law model fit parameters. See text for details.

TABLE 6  
RAYMOND-SMITH PLUS POWER-LAW AND DOUBLE  
RAYMOND-SMITH MEAN FIT PARAMETERS

Parameter	$\mu(\sigma_\mu)^a$	$\mu(\sigma_\mu)^b$
$N_H$ ( $\times 10^{20}$ cm $^{-2}$ )	4.9 (4.9)	4.6 (4.0)
$kT$ (keV)	0.70 (0.10)	0.69 (0.08)
$A(/A_\odot)$	0.043 (0.028)	0.043 (0.028)
$N_{H,2}$ ( $\times 10^{22}$ cm $^{-2}$ ) <sup>c</sup>	1.2 (1.4)	1.4 (2.1)
$\Gamma$ or $kT_2$ (keV)	1.71 (0.41)	5.3 (3.2)
$A_2$ ( $/A_\odot$ )	...	0.19 (0.18)

<sup>a</sup>Statistically-weighted mean of Raymond-Smith plus power-law fit parameters, with statistically-weight standard deviation given in parenthesis

<sup>b</sup>As in <sup>a</sup>, but for double Raymond-Smith fit

<sup>c</sup>Absorption applied only to hard (i.e., power-law or second Raymond-Smith) component

component model consisting of a “soft” Raymond-Smith plasma component and a “hard” power-law component. The results of fitting this model to the *ASCA* spectra are given in Table 5. In these fits the overall abundance was allowed to vary while individual abundances were fixed at solar ratios. Figures showing the model fits with residuals are given in Figure 2. “Weighted” histograms for the model parameters are shown in Figure 3. In these histograms, the area occupied by each data point is held constant while the width is proportional to the statistical error of the parameter. In this way poorly-constrained parameters do not bias the histograms significantly. Evidently, the soft-component temperature is rather narrowly distributed near  $kT \sim 0.7$  keV. Table 6 gives the statistically-weighted mean and standard deviation of each fit parameter, also showing the narrow distribution

of soft-component temperature. Also note that the mean value of the hard-component slope is  $\sim 1.7$ , similar to the values of  $\sim 1.7$ – $2.0$  observed in “normal” Seyfert 1 galaxies (c.f., Mushotzky, Done & Pounds 1993).

In order to check whether the X-ray spectra could be fit just as well by any two-component model, double power-law fits were also attempted. However, in every case, the resultant  $\chi^2$  was significantly higher, implying that the Raymond-Smith plus power-law model is preferred at better than 99% confidence (for all of the S0-3, local background fits with the exception of NGC 3147, where two components are not required). Additionally, a double Raymond-Smith fit was attempted. Here the improvement in  $\chi^2$  over the Raymond-Smith plus power-law fits (with one additional parameter, namely the hard-component abundance) was significant only

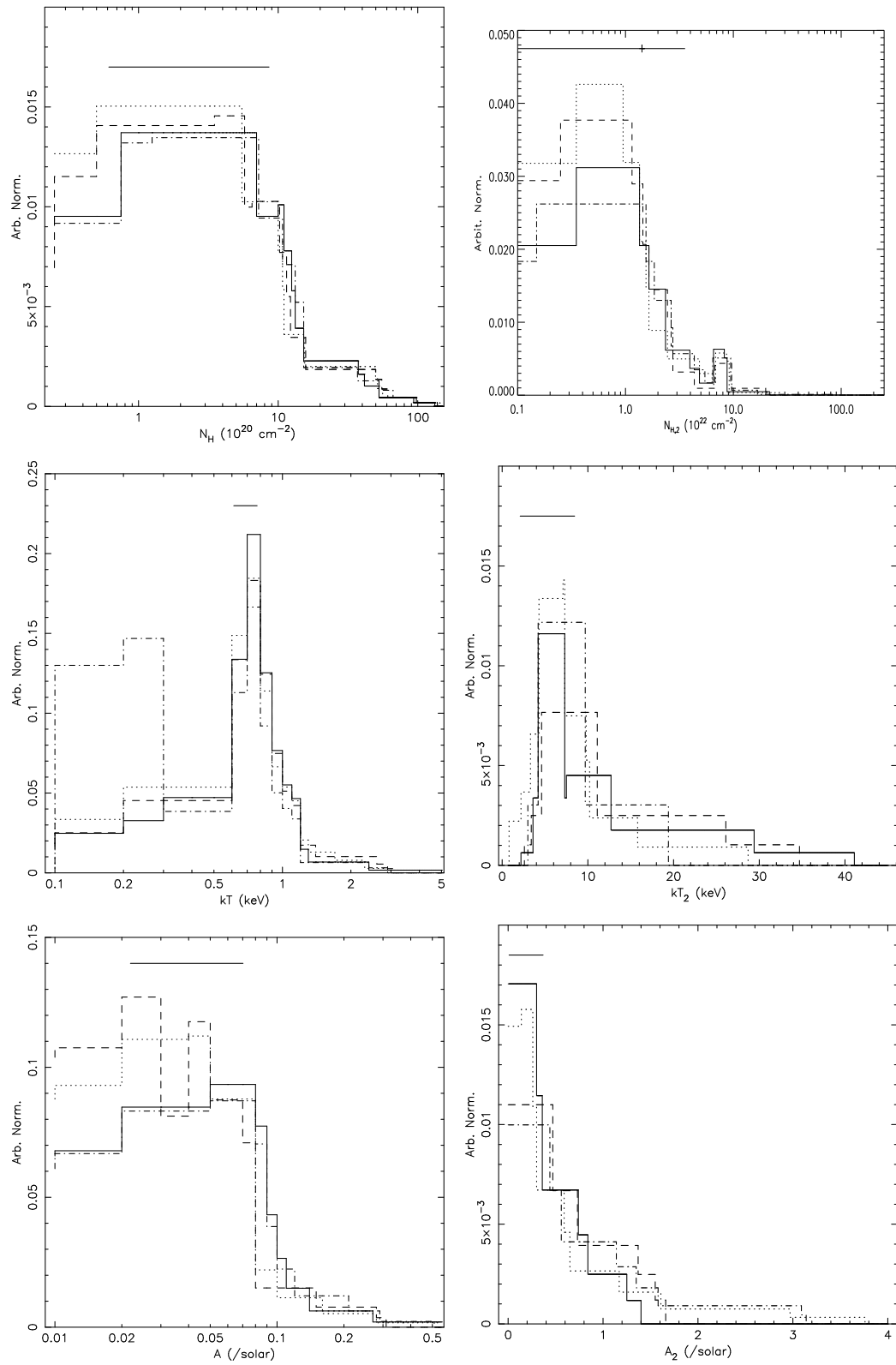


Fig. 4.— As in figure 3 but for the double Raymond-Smith fits.

in the cases of M82 and NGC 4258. This is principally due to the fact that in these cases there is significant line emission near the ionized Fe-K line energies of 6.7-6.9 keV (see also §6.4). In other cases no significant line emission is present near 6.7 keV, and the signal-to-noise ratio is not sufficient to distinguish a non-thermal from a thermal continuum model for the hard (i.e., 2-10 keV) component. “Weighted” histograms of the fits parameters are shown in Figure 4.

Table 6 also shows the statistically-weighted mean and standard deviation of the double Raymond-Smith fits. Evidently, the soft component parameters do not depend strongly on choice of hard-component model. This is shown graphically in Figure 5 which shows correlations of the common parameters (i.e.,  $N_H$ ,  $kT$  and  $A$  (from the soft-component in the case of the double Raymond-Smith fits), and the (additional) absorption applied to the hard component. However, note that the soft-component abundances may nevertheless have large systematic errors since there is no reason to assume *a priori* that the soft-component is *entirely* thermal. Any additional contribution to the 0.5-2.0 continuum that is not explicitly taken into account in these fits would act to reduce the *observed* equivalent widths and hence the abundance. This is one possible explanation for the unusually low abundances observed in these galaxies since starburst activity is likely to enrich the interstellar medium with the heavy metals that dominate X-ray spectra (see below for a more detailed discussion of the abundances). In addition, it is likely that there are multiple temperatures (and/or a temperature gradient) present in any X-ray emitting gas. However, since the signal-to-noise in most of the galaxies in this sample do not warrant fits

with more than two components, this possibility can only be examined in detail in a few objects (e.g., M82 in Ptak et al. 1997, Tsuru et al. (1997), and Moran & Lehnert 1997).

In the cases of NGC 253, NGC 4258, M51 and M82, it is clear from Figure 2 that significant sharp spectral features remain below  $\sim 2.5$  keV implying that modeling the soft flux with a single plasma with relative abundances (i.e., Fe/O) at the solar ratios is clearly too simple. Since the strongest line emission expected is Fe-L emission around 1 keV, it is likely that the overall abundance determination is dominated by the Fe abundance inferred from the Fe-L complex. Accordingly, for these galaxies additional fits were attempted in which the Fe abundance was allowed to vary independently from the other elements. The results are shown in Table 7 where the Fe abundance relative to the other heavy elements (dominated by the  $\alpha$ -burning elements O, Mg, S and Si) tend to be lower than the solar ratio by factors of 2-4. A similar low relative abundance of Fe was observed in more detailed spectral fitting of M82 and NGC 253 (Ptak et al. 1997) where other abundance ratios were allowed vary, and in Tsuru et al. (1997) where three-component fits were attempted to M82. In the case of these galaxies, the Fe abundance is depressed relative to the  $\alpha$ -process elemental abundances by factors of 5 or more, although as discussed in §6.7, this effect is diminished when a multiple-temperature model is fit to the data.

Allowing the oxygen abundance to be free results in a statistically significant improvement in  $\chi^2$  in NGC 4258 and M51, which are “Seyfert 2” galaxies, but *not* in M82 and NGC 253, which are “starburst” galaxies. While these fits are probably too simplistic to be



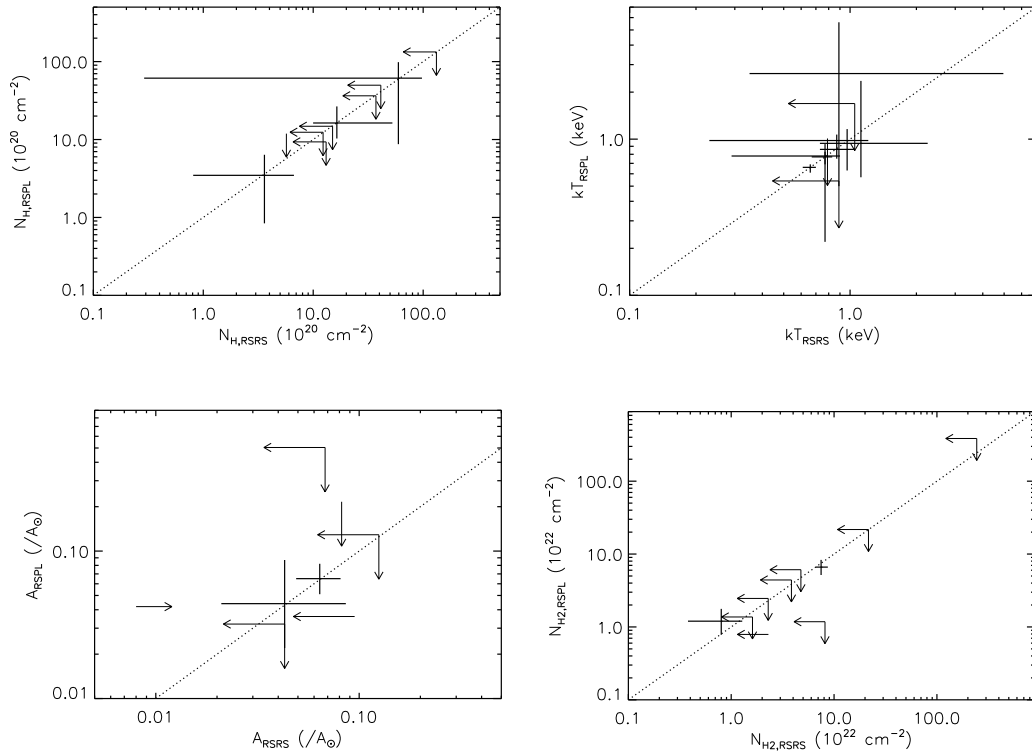


Fig. 5.— Comparison of the best-fit values for  $N_H$ ,  $kT$ ,  $A$  (abundance), and  $N_{H,2}$  (absorption applied only to the power-law component, in excess of the  $N_H$  column density applied to the entire model) from the Raymond-Smith plus power-law (“RSPL”) and double Raymond-Smith fits (“RSRS”).

taken too literally (i.e., the fits can be rejected statistically in all cases), *this result nevertheless implies a quantifiable difference in the starburst-like spectra of in Seyfert 2 and pure starburst galaxies.* We note that it would be unlikely for calibration errors to affect starbursts and Seyfert 2 galaxies differently, given the similarities in the overall shape of their spectrum. However, in order to determine to what extent these results may be biased by the SIS calibration uncertainties, the NGC 4258 and M51 SIS-only fits were repeated only using data in the 0.6-10.0 keV bandpass. In the case of NGC 4258, the best-fit oxygen abundance dropped from  $\sim 0.47$  to  $\sim 0.24$ , with the other fit parameters not changing significantly. The change in  $\chi^2$  for allowing the oxygen abundance to vary dropped from 23.0 to 4.3. In the case of M51, the oxygen abundance dropped to 0.02, while the Fe and remaining abundances were 0.025 and 0.094, respectively, similar to the values found for the fits in which the oxygen abundance was tied with the other abundances, and the change in  $\chi^2$  remained at  $\sim 8.6$ . Thus, this result is evidently more robust in the case of M51. To check the statistical significance of the overabundance of oxygen in the case of NGC 4258, we simulated source and background SIS spectra using the best-fitting model with the oxygen abundance left free, and repeated the fitting process. We found that the oxygen abundance was found to be three or more times the Fe abundance  $\sim 90\%$  of the time, and two or more times the “other” abundances  $\sim 68\%$  ( $1\sigma$ ) of the time. Incidentally, these simulations also showed that the statistical errors on the fits with the oxygen and iron abundance left free are approximately 1/2 of the values shown in Table 7, indicating that the confidence limits given in this paper are

conservative.

### 6.3. *ROSAT* PSPC and *ASCA* Fits

While the *ROSAT* PSPC has limited spectral resolution, as mentioned above its sensitivity in the 0.1-0.3 keV range and the presence of the large carbon edge results in a higher level of accuracy in determining absorption columns on the order of  $10^{19-20}\text{cm}^{-2}$ . Accordingly, simultaneous fits were attempted with *ASCA* and PSPC spectra. Separate PSPC observations existed in several cases (see Table 2) and these were not combined as an attempt to observe any long-term variability. For each galaxy two sets of PSPC spectra were extracted - one with the same region size as the *ASCA* SIS source region and one with a 1.25' source region. A 1.25' region is appropriate for a point-source observation (in the case of off-axis PSPC observation “ancillary” responses were created to compensate for the loss of flux due to vignetting and blurring of the point-spread function). Hereafter the 1.25' spectra are denoted “nuclear” since they are dominated by nuclear flux, while the “*ASCA*”-sized source regions should result in roughly the same flux as the *ASCA* fits (unless the galaxy’s X-ray flux is significantly extended beyond several arcminutes or the X-ray flux varied between the *ASCA* and *ROSAT* observations). The results are shown in Table 8 (the results of the S0-3 only, “local” background fits from Table 5 are shown for comparison) and Figure 6. As expected, the addition of the PSPC spectra resulted in significantly smaller errors on the column density while the other fit parameters were not impacted significantly. Note that systematic offsets on the order of  $\sim 15\%$  between the *ASCA* SIS and PSPC are apparent in the residuals shown in Figure 6. In most cases

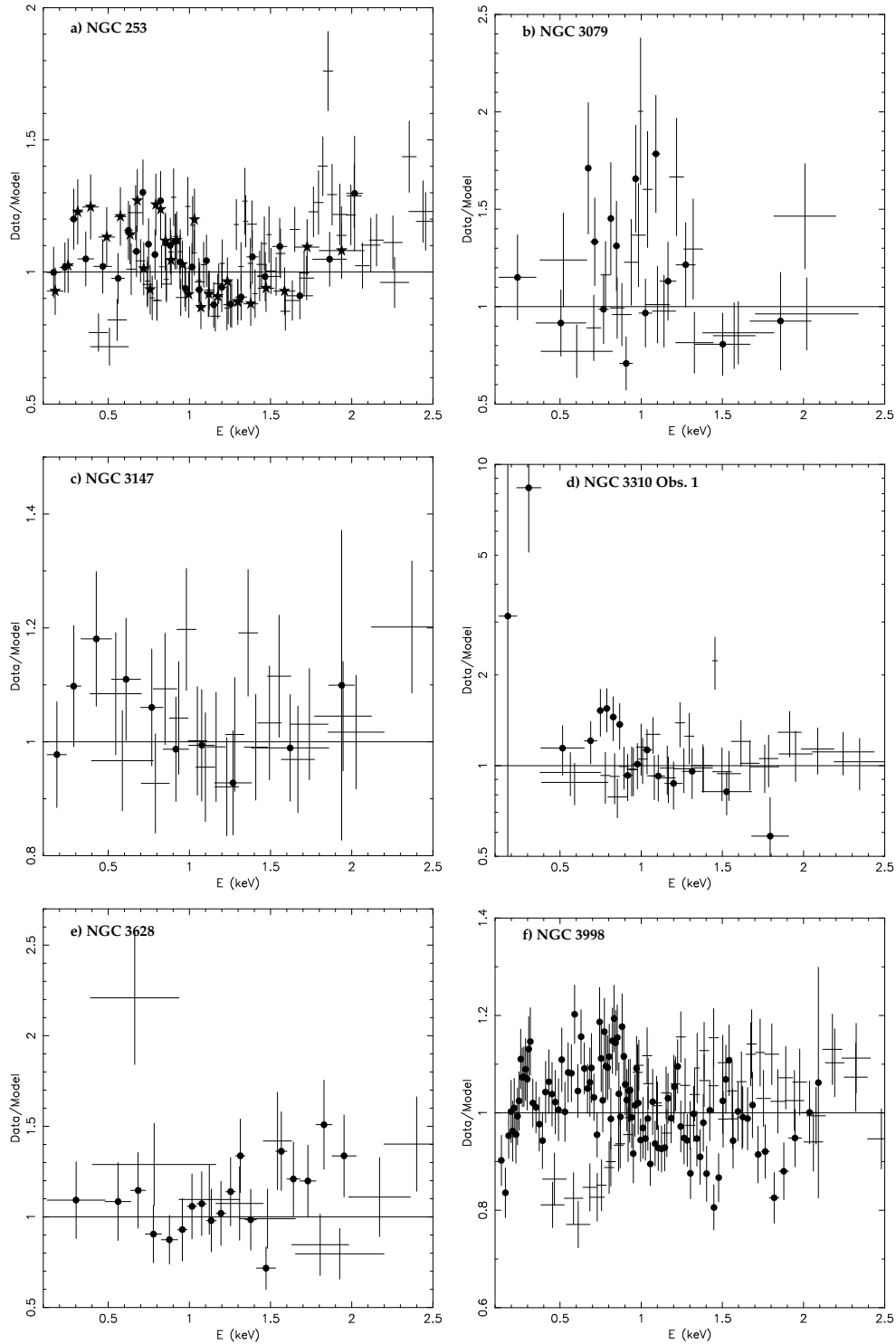


Fig. 6.— Ratio of data to model for Raymond-Smith plus Power-law fits to *ASCA* and *ROSAT* PSPC spectra. Only the energy range where *ASCA* and *ROSAT* overlap is shown. The PSPC points are marked with filled circles (in cases where more than one PSPC data set is available, the additional data points are marked with filled stars).

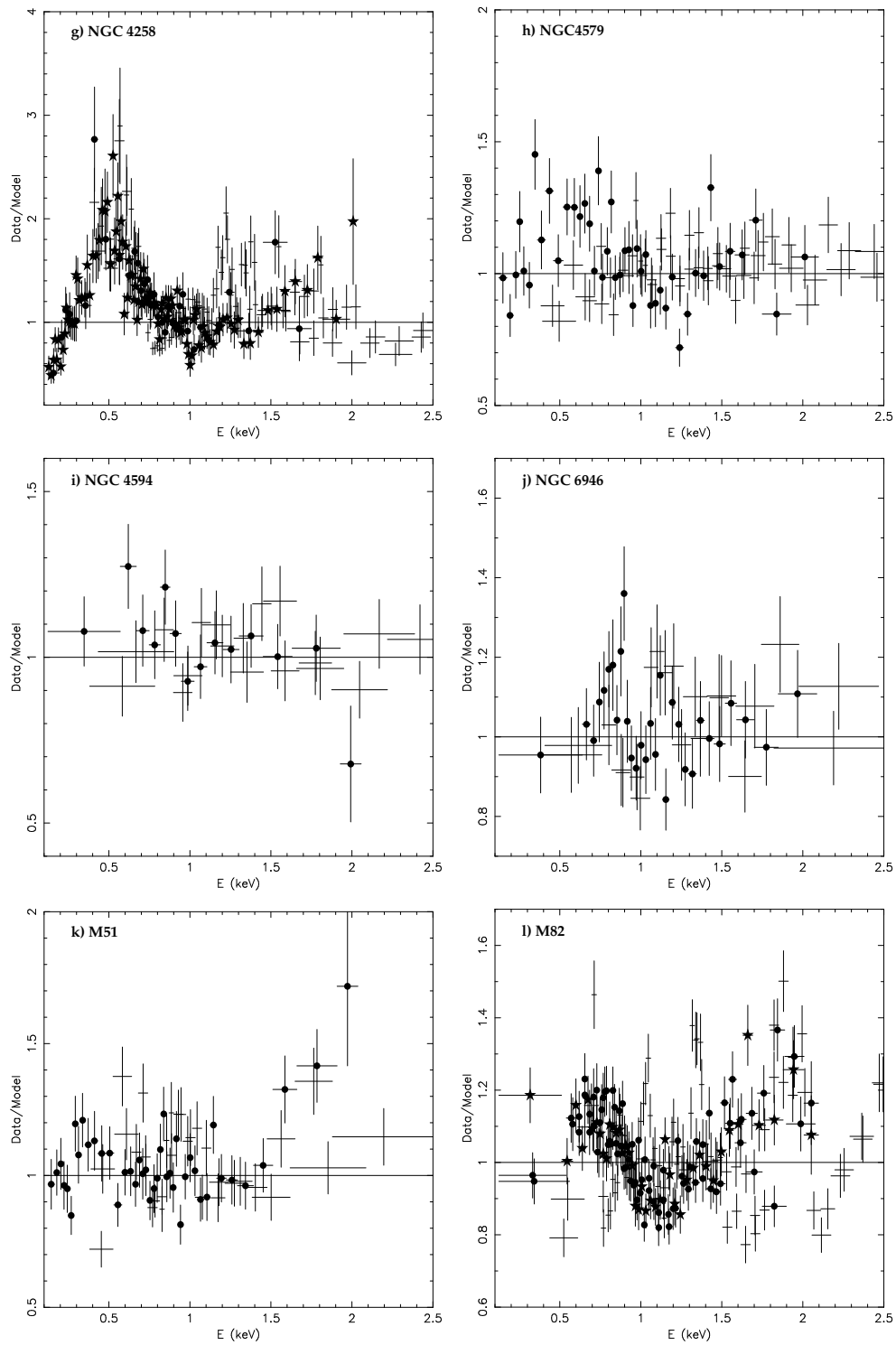


Fig. 6.— (cont.) *ASCA* and *ROSAT* Raymond-Smith plus Power-Law Fits

the statistical errors dominate this systematic error. These offsets are probably dominated by error in the calibration of the PSPC, since they are present present above 0.6 keV (the SIS calibration is most suspect below 0.6 keV, however see §6.7), where the SIS calibration is on the order of 6% (Orr et al. (1998); also note that version 4.0 of FTOOLS was used in this analysis, which underestimated spectral corrections to PSPC spectra). The discrepancy is particularly acute in the case of NGC 3998, and it is possible that the column density varied between the *ROSAT* and *ASCA* observations in this case. Table 9 gives the ratio of the 0.5-2.0 keV fluxes inferred from the PSPC spectra relative to the *ASCA* spectra. The variation in the flux inferred from each *ASCA* detector is shown to give an indication of the accuracy of the *ASCA* fluxes. There are clear variations present among the *ASCA* and *ROSAT* fluxes (particularly in the cases of NGC 3628 and NGC 4579) and among the “nuclear” and “*ASCA*”-region PSPC fluxes (indicating a 0.5-2.0 keV spatial extent in excess of 1.25’).

Since the addition of the PSPC data did not change the best-fit temperature determination, it is highly unlikely that the clustering of temperatures around the mean of 0.7 keV is due simply to a bandpass effect (i.e., the PSPC data is extending the bandpass from 0.4 keV to 0.1 keV). In galaxies where the best-fit temperature does change, either the Raymond-Smith component is not very significant (e.g., NGC 3147) or it appears that the true variation is in the best fit  $N_H$ , and the temperature is changing due to a correlation between temperature and  $N_H$ . Note that the change in  $N_H$  in these cases may not necessarily be real, but rather is indicative of flux below 0.4 keV that is detected by *ROSAT*. In-

deed, in every case where  $N_H$  changes with the addition of PSPC data,  $N_H$  decreases. This flux is most likely due to halo gas at  $\sim 0.3$  keV which is also occasionally dominates the *ASCA*-only fits (c.f., NGC 3079). Another indication that the clustering around the temperature of 0.7 keV (and secondarily around 0.3 keV) is not a bandpass effect is that in most cases the best-fit temperatures are fairly well constrained, which would not be the case otherwise.

#### 6.4. Fe-K Emission

In order to search for Fe-K emission, commonly observed in “normal” Seyfert galaxies, the *ASCA* spectra were fit in the 3-10 keV range with a simple power-law where the hard-component dominates. Initially a narrow Gaussian was introduced, fixed at 6.4 keV (appropriate for Fe less ionized the Fe XVI) and at 6.7 keV (appropriate for He-like Fe, the ionization state expected at the temperatures implied by the hard component of the double Raymond-Smith fits). In the cases where the Gaussian significantly reduced  $\chi^2$  the centroid and physical width ( $\sigma$ ) of the Gaussian was allowed to be a free parameter. The results are shown in Table 10 (which give 90% confidence upper-limits for galaxies with no significant Fe-K emission). Significant Fe-K emission was detected in five galaxies: M51 (see also Terashima et al. 1998a), M82 (see also Ptak et al. 1997), NGC 3147 (see also Ptak et al. 1996), NGC 4579 (see also Terashima et al. 1998b), and NGC 4258 (see also Makishima et al. 1994). See Paper II for a discussion of the implications of the presence or lack of Fe-K emission in these galaxies.

TABLE 11  
IONIZED OXYGEN ABSORPTION EDGE SEARCH

Galaxy	Fit*	$\tau_{\text{OVII}}$ (0.74 keV)	$\tau_{\text{OVIII}}$ (0.87 keV)
NGC 3147	S0-1, PL	<0.20	<0.13
	S0-3, PL	<0.16	<0.10
NGC 3998	S0-1, PL	0.13 (0.006-0.26)	0.08 (<0.20)
	S0-3, PL	0.07 (<0.19)	0.01 (<0.11)
NGC 4579	S0-1, PL	<0.04	<0.04
	S0-1, RS + PL	0.14 (<1.78)	<0.62

\*Fit used in oxygen edge search; PL = power-law-only model, RS + PL = Raymond-Smith + power-law model (both models include neutral absorption as discussed in §4.1-2).

## 6.5. Ionized Absorbers

Ionized, or “warm,” absorbers are frequently observed in Seyfert 1s as evidenced by the presence of O VII and OVIII absorption edges at 0.74 and 0.87 keV (see Reynolds 1997; George et al. 1997). Two good candidates for searching for a warm absorber in LINERs are NGC 3998 and NGC 4579. Both are broad-line LINERs, making them analogous to Seyfert 1s, and are among the brightest of the galaxies observed in this thesis. While also relatively bright, the soft flux in NGC 253, NGC 4258, M51 and M82 is dominated by thermal flux (note that this flux is often spatially as well as spectrally distinct from the hard flux). Table 11 shows the upper-limits on OVII and OVIII edges for these two galaxies obtained using the simple power-law fits (still including the neutral absorption). Since the presence of a soft component is significant in NGC 4579, the upper-limits were re-determined using the Raymond-Smith + power-law model discussed in §6.2, which re-

sulted in far less restrictive limits on the edges than the simple power-law model fits (as would be expected since the presences of the plasma flux “fills-in” the edges and reduces the contrast with the underlying continuum). Also, in Seyfert 2s where the X-ray emission is thought to be dominated by scattered flux, the scattering medium must be highly ionized. Here also absorption due to highly ionized oxygen might be observable. Accordingly, limits on OVII and OVIII were also determined for NGC 3147 (again using the power-law only model since the presence of a soft component is not highly significant).

## 6.6. Fluxes and Luminosities

The observed and intrinsic 0.4-10.0 keV fluxes for the *ASCA* spectra are given in Table 12. The S0-3, local background Raymond-Smith plus power-law fits and *ASCA* and *ROSAT* PSPC (with *ASCA* SIS source regions) simultaneous fits were used to determine the fluxes. The intrinsic fluxes were

determined by setting  $N_H$  and  $N_{H,2}$  to zero. As stated above, the values of  $N_H$  determined from the *ASCA* and PSPC simultaneous fits are more reliable than the values of  $N_H$  determined from the fits with *ASCA* data alone, so the unabsorbed fluxes from these fits are likewise more reliable. The contributions to the 0.4-10.0 keV flux from the Raymond-Smith and power-law components individually is also given. The significance of the improvement to  $\chi^2$  of the Raymond-Smith plus power-law fit over the power-law fit to the spectra from NGC 3147 is not large so the fluxes determined from the power-law fit is shown. Also, the flux from NGC 3310 does not extend beyond 1.25' and the "nuclear" PSPC spectrum has better signal-to-noise than the SIS-region PSPC spectrum, so the nuclear PSPC spectrum fit is also used in this case to determine the fluxes. This example also demonstrates how large the systematic error due to the specific choice of spectral model can be when estimating the unabsorbed flux of each component. The total observed 0.4-10.0 keV luminosity is also given in Table 12.

## 7. Complex Models

Here we investigate the results of fitting more complicated models to the spectra from brightest galaxies in our sample, NGC 253, NGC 4258, M51 and M82. Specifically, it is physically probable that the gas in these galaxies is not isothermal but rather has some temperature structure. Table 13 gives the results of double Raymond-Smith plus power-law fits. As discussed in Ptak et al. (1997) and DWM, the abundances inferred from spatially-averaged are somewhat model-dependent. Evidently, modeling the soft flux with even a crude temperature structure results in abso-

lute abundances that are no longer significantly subsolar, and in most cases, the underabundance of Fe relative to  $\alpha$ -process elements is no longer significant. For a detailed discussion of this issue, see DWM. Table 13 shows the results of restricting the SIS bandpass to 0.6-10.0 keV, and, with the exception of the NGC 253 fits, the results are comparable, indicating that these results, along with the simpler fits discussed previously, are not adversely affected by SIS calibration uncertainties below 0.6 keV.

Table 14 gives the results of fitting the *ASCA* and PSPC spectra from M82 with a plasma model with a power-law temperature dependence (a power-law continuum component is still included as well to fit the hard flux). However, we note that the temperatures inferred from a (relatively) simple Raymond-Smith plus power-law fit *does* adequately represent the average temperature of the X-ray emitting gas, and it is therefore of interest to discuss the thermodynamics implied by the Raymond-Smith plus power-law fits (see paper II). For example, we used the best-fitting model listed in Table 14 to simulate an SIS observation of M82, and fit the simulation with a single temperature plasma plus power-law model (with the Fe abundance allowed to vary). This resulted in a temperature of 0.66 keV, similar to the value listed in Table 7, where a single temperature plasma plus power-law model was fit of the actual SIS observation of M82. This is an important point for faint galaxies where more complex fits are not statistically warranted.

## 8. Summary

We have presented the results of a systematic analysis of the *ASCA* and *ROSAT* PSPC X-ray spectra from a sample of low-luminosity

TABLE 14  
POWER-LAW TEMPERATURE PLASMA PLUS POWER-LAW MODEL FIT TO M82

Fit Parameter	SIS Data Only	SIS + PSPC Data
$N_H$ ( $10^{21}$ cm $^{-2}$ )	2.9 (2.0-3.2)	1.1 (0.9-1.4)
kT $_{max}$ (keV)	1.10 (0.71-1.73)	1.12 (0.70-1.72)
$\alpha$	0.01 (<0.41)	0.44 (0.25-0.60)
$A$ ( $/A_\odot$ )	0.12 (<0.32)	0.49 (<2.4)
$A$ ( $/A_{\odot,O}$ )	0.14 (0.05-0.24)	1.1 (0.9-3.0)
$A$ ( $/A_{\odot,Mg}$ )	0.42 (0.25-0.62)	4.1 (0.9-9.6)
$A$ ( $/A_{\odot,Si}$ )	0.55 (0.38-0.73)	5.8 (>1.2)
$A$ ( $/A_{\odot,S}$ )	0.57 (>0.20)	4.5 (>2.0)
$A$ ( $/A_{\odot,Fe}$ )	0.12 (0.09-0.14)	1.2 (0.3-1.8)
$N_{H,2}$ ( $10^{22}$ cm $^{-2}$ )	1.7 (<2.9)	0.34 (0.08-0.62)
$\Gamma$	1.62 (1.55-1.73)	1.47 (1.33-1.55)
$\chi^2/\text{dof}$	479.5/384 (>99.9%)	1271/938 (>99.9%)

NOTE.—The soft-component model is a plasma consisting of a superposition of power-law distribution of temperatures. In practice, the model is computed discretely with the weighting of each temperature  $T$  being proportional to  $(\frac{T}{T_{max}})^\alpha$ . Elemental abundances that were allowed to vary freely of the others are specified.



AGN, LINERs and starbursts galaxies. The presence of at least two components appears to be universal for these types of galaxies. The “soft” component is well-described by a thermal plasma model with  $T \sim 10^7$  K while the “hard” component is well-described by an absorbed power-law. The hard component may also be due to a thermal bremsstrahlung component with  $T \sim 10^8$  K, however the soft component is inconsistent with a featureless continuum (i.e., a power-law or zero-abundance plasma model) at a high level of confidence. The relative strength of the hard and soft component varies from galaxy to galaxy, with the intrinsic 0.4-10.0 keV luminosity of the soft component typically being in the range of  $10^{39-40}$  ergs  $s^{-1}$  and the hard component typically being in the range of  $10^{40-41}$  ergs  $s^{-1}$ . The absolute abundances inferred from the soft-component fits tend to be significantly sub-solar, although the absolute abundances may be uncertain. In the galaxies with X-ray emission bright enough for individual abundances to be observed, the relative abundance of Fe to  $\alpha$ -process elements tend to be low (see also Ptak et al. 1997). There is some indication (at a low-statistical significance) that the abundance properties starburst emission from starburst galaxies differs from the starburst emission from low-luminosity AGN. Ionized absorption is not observed in these galaxies, in contrast to typical Seyfert 1 galaxies, although absorption edges may be “washed-out” by the soft component. Fe-K emission is detected in several galaxies. See Ptak (1997) and Ptak et al. (1998a,b) for a detailed discussion of these results. It is likely that detailed analysis of these galaxies by telescopes capable of (better) spatially-resolved broadband spectroscopy (i.e., *AXAF* and *XMM*) will considerably improve our understanding of the X-

ray emission from these galaxies.

A.P. wishes to thank the NASA GSRP program for support. This research made extensive use of the HEASARC (at NASA/GSFC), NASA’s Astrophysics Data System Abstract Service, and NED (at IPAC).

## REFERENCES

- Bhattacharya, D. et al. 1994, *ApJ*, 437, 173
- Boller, T. et al. 1992, *A&A*, 261, 57
- Bregman, J., Schulman, E., Tomisaka, K. 1995, *ApJ*, 439, 155
- Burnstein, D. & Heiles, C. 1984, *ApJS*, 54, 33
- Cash, W., 1979, *ApJ*, 228, 939
- Cecil, G., Wilson, A., De Pree, C. 1995, *ApJ*, 440, 181
- Cleary, M., et al. 1979, *A&AS*, 36, 95
- Collura, A., Reale, F., Schulman, E, Bregman, J. 1994, 420, 63L
- Dahlem, M., Heckman, T. & Fabbiano G. 1995, *ApJ*, 442, L49
- Dahlem, M. et al. 1996, *ApJ*, 461, 724
- Davidge, T. & Pritchett, C. 1990, *AJ*, 100, 102
- de Vaucouleurs, G. 1963, *ApJ*, 137, 720
- de Vaucouleurs, G., et al. 1991, *Third Reference Catalogue of Bright Galaxies* (New York: Springer-Verlag)
- Dressel, L. & Wilson, A. 1985, *ApJ*, 291, 668
- Fabbiano, G., Feigelson, E. & Zamorani, G. 1982, *ApJ*, 256, 397

- Fabbiano, G. & Trinchieri, G. 1984, ApJ, 286, 491
- Fabbiano, G & Trinchieri, G. 1987, ApJ, 315, 46
- Fabbiano, G. 1988, ApJ, 325, 544
- Fabbiano, G. 1989, ARA&A, 27, 87
- Fabbiano, G. et al. 1992, ApJS, 80, 531
- Freedman, W., et al. 1994, ApJ, 427, 628
- Fabbiano, G. & Juda, J. 1997, ApJ, 476, 666
- Goldshmidt O. & Raphaeli, Y. 1995, ApJ, 444, 113
- Green, P., Anderson, S., & Ward, M. 1992, MNRAS, 254, 30
- Greenhill, L. et al. 1995, ApJ, 400, 540
- Hartmann, D., & Burton, W. 1997, In *The Leiden-Dwingeloo Atlas of Galactic Neutral Hydrogen* (Cambridge: Cambridge University Press, UK)
- Kormendy, J. & Richstone, D. 1995, ARA&A, 33, 581
- Marston, A. et al. 1995, ApJ, 438, 663
- Makishima, K. et al. 1994, PASJ, 46, L77
- Moran, E., Halpern, J., & Helfand, D. 1994, ApJ, 433, L65
- Moran, E. 1996, ApJS, 106, 341
- Moran, E. & Lehnert, M. 1997, ApJ, 478, 172
- Mushotzky, R., Done, C., & Pounds, K. 1993, ARA&A, 717
- Neufeld, D. & Maloney, P. 1995, ApJ, 447, L17
- Ohashi et al. 1990, ApJ, 365, 180
- Ohashi, T & Tsuru, T. 1992, in *Frontiers of X-ray Astronomy*, eds. Y. Tanaka and K. Koyama, p. 435
- Orr, A., Yaqoob, T., Parmar, A., Piro, L., White, N., & Grandi, P. 1998, A&A, submitted
- Palumbo, G., Fabbiano, P., Fransson, C., & Trinchieri, G. 1985, ApJ, 298, 259
- Petre, R. 1993, in *The Nearest Active Galaxies*, eds. J. Beckman, L. Colina, and H. Netzer, 117
- Pietsch, W. 1995, Adv. Sp. Res., 16, 155
- Ptak, A., Yaqoob, T., Serlemitsos, P., Kunieda, H., & Terashima, Y. 1996, ApJ, 459, 542
- Ptak, A. 1997, *Ph. D. thesis*, University of Maryland
- Ptak, A., Serlemitsos, P., Yaqoob, T., Mushotzky, R., & Tsuru, T. 1997, AJ, 113, 1286
- Ptak, A., Yaqoob, T., Mushotzky, R., Serlemitsos, P. & Griffiths, R. 1998, ApJ, submitted
- Ptak, A., Yaqoob, T., Serlemitsos, P. & Mushotzky, R., ApJ, in preparation
- Read, A., Ponman, T., & Strickland, D. 1997, MNRAS, 286, 626
- Reichert, G., Mushotzky, R., & Filippenko, A. 1994, in *The Soft X-ray Cosmos*, eds. E. Schlegel and R. Petre, 85
- Rephaeli, Y., Gruber, D., Persic, M. 1995, A&A, 300,91

- Schaaf, R. et al. 1989, ApJ, 336, 722
- Schlegel, E. 1994a, ApJ, 424, 99L
- Schlegel, E. 1994b, ApJ, 434, 523
- Soifer, B. T., et al. 1987, ApJ, 320, 238
- Stark, A., et al. 1992, ApJS, 79, 77
- Tanaka, Y., Inoue, H., & S. Holt 1994, PASJ, 46, L37
- Terashima, Y. et al. 1998, ApJ, in press
- Terashima, Y. et al. 1998, ApJ, in press
- Tsuru, T. et al. 1990, PASJ, 42, L75
- Tsuru, T., Awakim H., Koyoma, K., & Ptak, A. 1997, PASJ, 49, 619
- Tully, R. 1988, Nearby Galaxy Catalog (Cambridge University Press)
- Yaqoob et al. 1995, ApJ, 455, 508
- Watson, M., Stanger, V. & Griffiths, R. 1984, ApJ, 286, 144
- Zezas, A., Georgantopoulos, I. & Ward, M. 1998, MNRAS, in press

TABLE 4  
SIMPLE POWER-LAW FITS TO *ASCA* SPECTRA

Galaxy	Detectors	Background*	$N_H$ ( $10^{20}$ cm $^{-2}$ )	$\Gamma$	$\chi^2/\text{dof}$
NGC 253	S0-1	L	6.79 (5.12-8.53)	1.85 (1.79-1.91)	581.3/296 (>99.9%)
		B	5.22 (3.70-6.79)	1.82 (1.77-1.88)	599.0/296 (>99.9%)
	S0-3	L	7.22 (5.72-8.79)	1.86 (1.82-1.91)	984.2/681 (>99.9%)
		B	5.84 (4.48-7.25)	1.85 (1.81-1.89)	1038.7/681 (>99.9%)
NGC 3079	S0-1	L	7.68 (0.09-17.50)	2.61 (2.15-3.24)	176.5/122 (>99.9%)
		B	2.82 (<9.19)	2.50 (2.21-2.93)	257.4/122 (>99.9%)
	S0-3	L	4.45 (<11.60)	2.40 (2.08-2.80)	305.0/233 (99.9%)
		B	0.69 (<5.69)	2.35 (2.18-2.66)	371.9/233 (>99.9%)
NGC 3147	S0-1	L	0.00 (<3.62)	1.70 (1.63-1.83)	166.5/151 (81.6%)
		B	0.00 (<1.56)	1.78 (1.71-1.86)	168.4/151 (84.2%)
	S0-3	L	0.00 (<3.14)	1.72 (1.66-1.81)	357.4/357 (51.6%)
		B	0.00 (<2.24)	1.81 (1.75-1.89)	353.4/357 (45.6%)
NGC 3310 (Obs. 1)	S0-1	L	7.98 (2.86-13.80)	1.81 (1.63-2.01)	138.7/103 (98.9%)
		B	5.29 (1.29-9.71)	1.75 (1.60-1.92)	147.0/103 (99.7%)
	S0-3	L	7.14 (2.70-12.20)	1.79 (1.65-1.94)	249.3/193 (99.6%)
		B	5.74 (2.15-9.70)	1.79 (1.67-1.92)	277.5/193 (>99.9%)
NGC 3310 (Obs. 2)	S0-1	L	5.09 (<13.00)	1.69 (1.47-1.94)	68.4/65 (63.7%)
	S0-3	L	5.07 (<12.20)	1.71 (1.53-1.90)	120.4/118 (57.9%)
NGC 3310 (Obs. 3)	S0-1	L	9.18 (1.33-18.50)	1.71 (1.49-1.96)	71.5/65 (72.9%)
	S0-3	L	8.50 (1.65-16.60)	1.72 (1.54-1.90)	148.2/122 (94.7%)
NGC 3628	S0-1	L	1.09 (<16.70)	1.06 (0.88-1.33)	43.7/42 (60.1%)
		B	0.76 (<16.40)	1.08 (0.91-1.37)	44.9/42 (64.9%)
	S0-3	L	7.03 (<25.90)	1.15 (0.96-1.38)	81.3/77 (65.3%)
		B	9.05 (<30.40)	1.22 (1.01-1.47)	88.7/77 (82.9%)
NGC 3998	S0-1	L	8.93 (7.49-10.40)	1.89 (1.84-1.93)	287.6/328 (5.3%)
		B	8.94 (7.58-10.40)	1.90 (1.85-1.94)	291.8/328 (7.5%)
	S0-3	L	8.83 (7.57-10.10)	1.89 (1.86-1.93)	819.4/836 (34.7%)
		B	8.90 (7.70-10.10)	1.90 (1.87-1.93)	837.3/836 (51.9%)
NGC 4258	S0-1	L	0.00 (<0.18)	1.92 (1.84-2.00)	3197.7/293 (>99.9%)
		B	0.00 (<0.18)	2.06 (1.99-2.13)	3383.0/293 (>99.9%)
	S0-3	L	0.00 (<0.14)	0.86 (0.80-0.93)	4843.5/670 (>99.9%)
		B	0.00 (<0.13)	0.94 (0.88-1.01)	5435.0/670 (>99.9%)
NGC 4579	S0-1	L	7.38 (5.30-9.56)	1.87 (1.80-1.94)	319.4/255 (99.6%)
		B	8.51 (6.58-10.5)	1.91 (1.84-1.98)	357.4/255 (>99.9%)
	S0-3	L	6.40 (4.58-8.3)	1.83 (1.78-1.89)	655.7/599 (94.6%)
		B	8.40 (6.73-10.1)	1.92 (1.87-1.97)	686.0/599 (99.2%)
NGC 4594	S0-1	L	8.12 (3.90-12.7)	1.69 (1.57-1.82)	144.7/139 (64.7%)
		B	7.93 (4.07-12.1)	1.71 (1.60-1.83)	156.3/139 (85.0%)
	S0-3	L	8.68 (4.91-12.8)	1.72 (1.63-1.81)	284.4/283 (53.5%)
		B	9.53 (6.05-13.3)	1.69 (1.61-1.77)	292.9/283 (67.0%)
NGC 6946	S0-1	L	23.3 (18.9-28.1)	2.72 (2.55-2.92)	138.0/122 (84.7%)
		B	23.0 (18.7-27.6)	2.73 (2.56-2.92)	140.6/122 (88.0%)
	S0-3	L	22.3 (18.5-26.4)	2.72 (2.58-2.88)	317.6/261 (99.1%)
		B	23.4 (19.8-27.4)	2.79 (2.66-2.94)	320.8/261 (99.3%)
M51 (PV Obs.)	S0-1	L	16.0 (11.2-21.8)	3.62 (3.30-4.02)	750.7/151 (>99.9%)
		B	12.3 (8.3-17.0)	3.38 (3.11-3.70)	773.0/151 (>99.9%)
	S0-3	L	7.88 (4.76-11.4)	3.07 (2.87-3.30)	1096.5/329 (>99.9%)
		B	6.06 (3.33-9.06)	2.95 (2.77-3.15)	1112.2/329 (>99.9%)
M51 (AOI Obs.)	S0-1	L	3.49 (<12.2)	2.69 (2.40-3.16)	193.4/78 (>99.9%)
	S0-3	L	0.00 (<1.38)	2.42 (2.31-2.53)	453.1/269 (>99.9%)
M82	S0-1	L	7.72 (6.61-8.84)	1.75 (1.71-1.78)	2173.1/394 (>99.9%)
		B	6.25 (5.22-7.29)	1.73 (1.70-1.77)	2245.0/394 (>99.9%)
	S0-3	L	5.76 (4.86-6.68)	1.68 (1.66-1.70)	3150.6/1160 (>99.9%)
		B	4.43 (3.59-5.27)	1.67 (1.65-1.69)	3266.6/1160 (>99.9%)

\*Choice of background: L = "local" background determined from annular region around source; B = background determined from blank-sky events

TABLE 5  
RAYMOND-SMITH PLUS POWER-LAW FITS TO THE ASCA SPECTRA

Galaxy	Det.	Bgd. <sup>a</sup>	$N_H$ <sup>b</sup>	$kT$ (keV)	$A$ ( $/10^{-2} A_\odot$ )	$N_{H,PL}$ <sup>c</sup>	$\Gamma$	$\chi^2/\text{dof}$
NGC 253	S0-1	L	7.2 (<13.0)	0.78 (0.69-0.83)	4.2 (2.1-8.6)	1.17 (0.65-1.87)	2.02 (1.78-2.30)	385.9/292 (>99.9%)
		B	0.0 (<7.4)	0.69 (0.60-0.81)	500 (>37.2)	0.05 (<0.08)	1.68 (1.58-1.77)	417.4/292 (>99.9%)
	S0-3	L	6.7 (<12.4)	0.77 (0.69-0.83)	4.4 (2.2-8.7)	1.20 (0.78-1.77)	2.12 (1.95-2.32)	760.2/677 (98.6%)
		B	5.8 (<10.8)	0.77 (0.69-0.83)	3.9 (2.0-7.3)	1.25 (0.83-1.80)	2.11 (1.94-2.31)	805.2/677 (>99.9%)
NGC 3079	S0-1	L	61.8 (2.7-98.0)	0.14 (<0.52)	1.0 (<11.)	0.00 (<5.22)	2.05 (0.56-4.62)	128.3/118 (75.6%)
		B	31.3 (<71.3)	0.19 (0.11-0.91)	0.3 (<1.9)	0.00 (<3.07)	1.51 (-1.38-2.47)	184.0/118 (>99.9%)
	S0-3	L	61.3 (8.7-98.4)	0.14 (<0.54)	1.2 (<13.)	0.05 (<4.41)	2.20 (1.24-4.24)	251.9/229 (85.7%)
		B	32.2 (2.0-71.8)	0.18 (0.11-0.54)	0.4 (<2.1)	0.00 (<2.74)	1.68 (0.75-2.50)	294.0/229 (99.8%)
NGC 3147	S0-1	L	0.0 (<12.7)	0.89 (<4.49)	1.7 (<6.2)	0.42 (<53.80)	1.39 (-1.49-1.88)	160.3/147 (78.6%)
		B	0.1 (<13.0)	0.14 (<1.23)	500	0.02 (<0.14)	1.76 (1.60-1.98)	158.3/147 (75.2%)
	S0-3	L	0.0 (<9.3)	2.63 (0.50-5.60)	4.0 (<50.)	2.04 (<385)	0.23 (-2.34-1.71)	344.5/353 (38.3%)
		B	0.0 (<15.1)	0.13 (0.10-0.21)	500 (>1.0)	0.06 (<0.16)	1.86 (1.72-2.03)	343.8/353 (37.3%)
NGC 3310 Obs. 1	S0-1	L	16.8 (<35.8)	0.78 (<1.00)	3.5	2.87 (<7.03)	2.46 (1.35-4.11)	100.2/99 (55.3%)
		B	70.3 (13.8-100)	0.14 (<0.95)	2.6 (<38)	0.00 (<5.37)	1.94 (1.45-3.05)	101.1/99 (57.8%)
	S0-3	L	17.7 (<36.4)	0.78 (<1.01)	3.2	2.93 (<6.10)	2.35 (1.50-3.45)	204.5/189 (79.1%)
		B	14.0 (2.9-99.2)	0.78 (0.11-0.99)	2.5 (<09.4)	3.24 (0.90-6.26)	2.50 (1.70-3.52)	223.0/189 (95.4%)
NGC 3310 Obs. 2	S0-1	L	15.3 (<55.1)	0.65 (0.10-0.95)	3.7 (>0.1)	0.33 (<3.04)	1.35 (0.39-2.38)	48.1/61 (11.5%)
	S0-3	L	14.5 (<116)	0.65 (0.11-0.88)	4.2 (>0.2)	0.49 (<2.99)	1.59 (0.98-2.40)	100.0/114 (17.8%)
NGC 3310 Obs. 3	S0-1	L	78.2 (<113)	0.14 (<2.37)	8.4	0.17 (<5.85)	2.24 (1.49-3.85)	58.6/61 (43.7%)
	S0-3	L	84.4 (<129)	0.14 (<1.23)	7.7	0.14 (<5.59)	2.20 (1.64-3.51)	130.3/118 (79.3%)
NGC 3628	S0-1	L	90.9 (<141)	0.11 (<0.77)	500	0.02 (<1.53)	1.66 (0.95-2.66)	33.3/38 (31.4%)
		B	78.4 (<136)	0.11 (0.11-0.47)	500	0.10 (<1.41)	1.66 (0.93-2.63)	35.6/38 (41.9%)
	S0-3	L	88.6 (<133)	0.11 (<1.69)	500	0.12 (<1.18)	1.73 (1.23-2.38)	62.7/73 (20.0%)
		B	70.6 (<129)	0.13 (0.12-1.77)	500	0.38 (<1.27)	1.85 (1.30-2.52)	68.3/73 (36.6%)
NGC 3998	S0-1	L	5.9 (<12.7)	0.94 (0.46-4.91)	0.6 (<2.7)	0.71 (<1.57)	1.75 (-1.48-2.04)	271.8/324 (1.6%)
		B	6.0 (<12.3)	1.07 (0.53-4.54)	0.5 (<2.8)	0.71 (<1.32)	1.62 (-1.30-2.00)	273.6/324 (1.9%)
	S0-3	L	5.5 (<11.9)	0.94 (0.57-2.36)	0.8 (<3.2)	0.63 (<1.37)	1.71 (0.93-1.91)	805.9/832 (26.4%)
		B	6.2 (<12.8)	0.90 (0.52-1.69)	0.7 (<3.0)	0.67 (<1.36)	1.74 (1.20-1.96)	823.6/832 (42.5%)
NGC 4258	S0-1	L	3.5 (0.7-6.5)	0.66 (0.62-0.70)	6.6 (5.0-8.5)	5.73 (3.80-8.20)	0.88 (0.50-1.32)	417.9/289 (>99.9%)
		B	25.9 (18.2-35.1)	0.30 (0.25-0.37)	2.1 (1.5-2.9)	2.25 (0.92-3.77)	0.48 (0.18-0.80)	438.7/289 (>99.9%)
	S0-3	L	3.5 (0.8-6.4)	0.66 (0.61-0.69)	6.5 (5.1-8.2)	6.62 (5.16-8.32)	1.14 (0.89-1.41)	827.9/666 (>99.9%)
		B	2.5 (0.2-5.0)	0.65 (0.61-0.69)	5.3 (4.2-6.7)	7.12 (5.63-8.84)	1.19 (0.94-1.46)	882.8/666 (>99.9%)
NGC 4579	S0-1	L	1.6 (<14.7)	0.87 (0.76-1.06)	4.9 (0.9-14.)	0.32 (<2.71)	1.58 (1.27-1.84)	261.5/251 (68.9%)
		B	5.0 (<14.9)	0.92 (0.80-1.11)	4.0 (1.0-14.)	0.29 (<2.63)	1.44 (1.07-1.80)	282.4/251 (91.6%)
	S0-3	L	3.6 (<14.8)	0.86 (0.75-1.07)	4.2 (0.9-13.)	0.47 (<2.46)	1.59 (1.38-1.79)	587.5/595 (42.1%)
		B	2.1 (<15.3)	0.89 (0.80-1.09)	5.0 (1.0-22.)	0.26 (<2.67)	1.64 (1.36-1.87)	604.6/595 (61.6%)
NGC 4594	S0-1	L	0.0 (<98.1)	0.76 (0.15-0.89)	8.2 (<21.)	0.72 (<3.67)	1.88 (1.53-2.87)	112.0/135 (7.4%)
		B	0.0 (<51.7)	0.66 (0.24-0.84)	7.9 (0.2-19.)	0.46 (<3.13)	1.78 (1.46-2.66)	110.6/135 (6.1%)
	S0-3	L	0.0 (<49.8)	0.78 (0.22-0.93)	9.0 (<22.)	0.79 (0.27-3.35)	1.94 (1.67-2.72)	242.9/279 (5.8%)
		B	23.0 (<54.8)	0.62 (0.23-0.85)	1.9 (0.4-17.)	1.89 (0.35 - 3.33)	2.30 (1.78-2.83)	246.4/279 (7.9%)
NGC 6946	S0-1	L	18.6 (<74.7)	0.88 (0.15-1.27)	2.0	4.09 (<20.3)	2.45 (0.57-4.95)	110.7/118 (32.9%)
		B	16.0 (<68.6)	0.97 (0.16-1.26)	2.8 (<8.6)	4.05 (<20.8)	2.12 (0.39-5.43)	111.9/118 (35.9%)
	S0-3	L	16.3 (10.3-26.6)	0.98 (0.63-1.16)	3.6 (0.4-9.1)	5.70 (<21.7)	2.53 (1.25-5.13)	268.2/257 (69.7%)
		B	16.0 (10.5-24.9)	0.99 (0.67-1.24)	3.4 (0.4-8.2)	8.54 (2.03-36.3)	3.50 (1.90-8.18)	278.1/257 (82.5%)

TABLE 5—*Continued*

Galaxy	Det.	Bgd. <sup>a</sup>	$N_H^b$	$kT$ (keV)	$A$ ( $/10^{-2} A_\odot$ )	$N_{H,PL}^c$	$\Gamma$	$\chi^2/\text{dof}$
M51 PV Obs.	S0-1	L	17.3 (9.0-28.3)	0.32 (0.24-0.41)	2.1 (1.3-4.9)	1.63 (<3.64)	2.25 (1.18-3.35)	237.1/147 (>99.9%)
		B	16.7 (8.9-27.1)	0.31 (0.24-0.40)	1.9 (1.1-4.3)	1.56 (<3.40)	2.20 (1.21-3.18)	235.7/147 (>99.9%)
	S0-3	L	16.7 (8.6-27.0)	0.32 (0.25-0.41)	2.3 (1.4-4.7)	1.14 (<2.64)	1.90 (1.21-2.61)	439.8/325 (>99.9%)
		B	16.1 (8.5-26.0)	0.32 (0.25-0.40)	2.0 (1.3-4.2)	1.19 (<2.58)	1.98 (1.30-2.64)	444.3/325 (>99.9%)
M51 AO1 Obs.	S0-1	L	70.3 (<104)	0.14 (<0.86)	3.2	0.00 (<7.20)	1.93 (0.78-4.00)	78.7/74 (66.7%)
	S0-3	L	5.0 (<78.1)	0.66 (0.14-0.82)	4.0 (1.0-21.)	2.70 (<6.87)	1.78 (0.92-2.88)	253.2/265 (31.2%)
M82	S0-1	L	15.5 (9.8-19.5)	0.80 (0.77-0.82)	7.1 (5.2-11.)	1.15 (0.61-1.74)	1.59 (1.44-1.76)	826.4/390 (>99.9%)
		B	12.8 (7.8-16.3)	0.80 (0.78-0.83)	6.6 (4.9-9.6)	1.17 (0.67-1.74)	1.57 (1.43-1.73)	868.3/390 (>99.9%)
	S0-3	L	16.0 (10.9-19.8)	0.79 (0.75-0.81)	6.6 (4.9-9.6)	1.17 (0.73-1.63)	1.64 (1.55-1.75)	1650.7/1156 (>99.9%)
		B	13.3 (8.8-16.6)	0.79 (0.76-0.82)	6.1 (4.6-8.6)	1.21 (0.79-1.65)	1.64 (1.54-1.74)	1722.6/1156 (>99.9%)

<sup>a</sup>Choice of background: L = “local” background determined from annular region around source; B = background determined from blank-sky events

<sup>b</sup> $\times 10^{20} \text{ cm}^{-2}$ , applied to both spectral components

<sup>c</sup> $\times 10^{22} \text{ cm}^{-2}$ , applied only to the power-law component

TABLE 7  
VARIABLE FE & O ABUNDANCE FITS

Fit Parameter	Fe free, S0-1	Fe free, S0-3	O & Fe free, S0-1	O & Fe free, S0-3
NGC 253				
$N_H$ ( $10^{20}$ cm $^{-2}$ )	5.42 (<13.9)	5.63 (<13.3)	5.53 (<14.70)	5.89 (<14.10)
kT (keV)	0.65 (0.55-0.75)	0.66 (0.56-0.75)	0.66 (0.46-0.79)	0.66 (0.51-0.78)
$A$ ( $/A_{\odot}$ )	0.260 (0.112-0.654)	0.260 (0.120-0.645)	0.257 (0.102-0.706)	0.254 (0.109-0.691)
$A$ ( $/A_{\odot, O}$ )	...	...	0.265 (0.067-0.758)	0.267 (0.074-0.746)
$A$ ( $/A_{\odot, Fe}$ )	0.041 (0.016-0.098)	0.041 (0.018-0.097)	0.041 (0.015-0.102)	0.040 (0.017-0.101)
$N_{H,2}$ ( $10^{22}$ cm $^{-2}$ )	1.02 (0.54-1.82)	1.14 (0.71-1.78)	1.03 (0.51-1.92)	1.15 (0.69-1.87)
$\Gamma$	2.03 (1.78-2.35)	2.14 (1.95-2.38)	2.03 (1.76-2.38)	2.14 (1.94-2.39)
$\chi^2/\text{dof}$	331.8/291 (95.0%)	699.8/676 (74.5%)	331.8/290 (95.4%)	699.8/673 (77.0%)
NGC 4258				
$N_H$ ( $10^{20}$ cm $^{-2}$ )	1.92 (<5.86)	1.84 (<5.43)	2.77 (<6.75)	2.79 (<6.64)
kT (keV)	0.62 (0.32-0.67)	0.62 (0.49-0.67)	0.67 (0.60-0.75)	0.67 (0.60-0.73)
$A$ ( $/A_{\odot}$ )	0.234 (0.124-0.422)	0.225 (0.122-0.396)	0.154 (0.038-0.331)	0.155 (0.046-0.318)
$A$ ( $/A_{\odot, O}$ )	...	...	0.468 (0.226-0.861)	0.481 (0.239-0.876)
$A$ ( $/A_{\odot, Fe}$ )	0.075 (0.034-0.111)	0.074 (0.052-0.106)	0.087 (0.059-0.126)	0.086 (0.061-0.122)
$N_{H,2}$ ( $10^{22}$ cm $^{-2}$ )	5.27 (3.30-7.81)	6.26 (4.74-8.05)	5.89 (3.65-8.85)	6.84 (5.13-8.87)
$\Gamma$	0.84 (0.44-1.29)	1.11 (0.84-1.40)	0.90 (0.47-1.41)	1.17 (0.88-1.48)
$\chi^2/\text{dof}$	384.3/288 (99.9%)	793.6/665 (>99.9%)	364.0/287 (99.9%)	769.8/662 (99.8%)
M51, PV Obs.				
$N_H$ ( $10^{20}$ cm $^{-2}$ )	7.10 (<17.40)	6.55 (<16.30)	1.51 (<15.60)	2.79 (<16.00)
kT (keV)	0.41 (0.32-0.55)	0.41 (0.33-0.55)	0.37 (0.28-0.46)	0.37 (0.28-0.46)
$A$ ( $/A_{\odot}$ )	0.098 (0.035-0.278)	0.103 (0.039-0.280)	0.351 (>0.051)	0.251 (0.052-16.700)
$A$ ( $/A_{\odot, O}$ )	...	...	0.172 (>0.023)	0.130 (0.024-6.590)
$A$ ( $/A_{\odot, Fe}$ )	0.032 (0.017-0.160)	0.033 (0.019-0.126)	0.103 (>0.020)	0.075 (0.022-4.700)
$N_{H,2}$ ( $10^{22}$ cm $^{-2}$ )	1.65 (<4.09)	1.28 (<3.06)	0.00 (<3.15)	0.00 (<2.36)
$\Gamma$	2.08 (1.02-3.33)	1.79 (1.09-2.58)	1.65 (1.12-2.98)	1.54 (1.16-2.36)
$\chi^2/\text{dof}$	212.8/146 (>99.9%)	412.9/324 (>99.9%)	204.2/145 (99.9%)	404.0/321 (99.9%)
M82				
$N_H$ ( $10^{20}$ cm $^{-2}$ )	20.1 (15.7-23.9)	19.9 (16.1-23.5)	19.50 (14.10-23.90)	19.60 (14.70-24.20)
kT (keV)	0.65 (0.60-0.69)	0.65 (0.60-0.69)	0.64 (0.59-0.69)	0.65 (0.60-0.69)
$A$ ( $/A_{\odot}$ )	0.291 (0.210-0.429)	0.303 (0.224-0.430)	0.294 (0.211-0.452)	0.304 (0.220-0.449)
$A$ ( $/A_{\odot, O}$ )	...	...	0.255 (0.125-0.450)	0.285 (0.140-0.507)
$A$ ( $/A_{\odot, Fe}$ )	0.046 (0.033-0.069)	0.048 (0.035-0.068)	0.045 (0.032-0.069)	0.047 (0.034-0.069)
$N_{H,2}$ ( $10^{22}$ cm $^{-2}$ )	1.54 (0.96-2.13)	1.51 (1.09-1.94)	1.49 (0.88-2.11)	1.49 (1.02-1.98)
$\Gamma$	1.73 (1.54-1.93)	1.76 (1.64-1.88)	1.72 (1.53-1.92)	1.75 (1.63-1.89)
$\chi^2/\text{dof}$	582.2/389 (>99.9%)	1344.7/1155 (>99.9%)	581.4/388 (>99.9%)	1344.5/1152 (>99.9%)

TABLE 8  
SIMULTANEOUS *ASCA* & *ROSAT* PSPC SPECTRAL FITS

Galaxy	Dets.	$N_H$ ( $10^{20}$ cm $^{-2}$ )	kT (keV)	$A$ ( $/10^{-2} A_\odot$ )	$N_{H,2}$ ( $10^{22}$ cm $^{-2}$ )	$\Gamma$	$\chi^2/\text{dof}$
NGC 253	S0-3	6.72 (<12.4)	0.77 (0.69-0.83)	4.4 (2.2-8.7)	1.20 (0.78-1.77)	2.12 (1.95-2.32)	760.2/677 (98.6%)
	S0-3, PSPC <sup>a</sup>	0.49 (<2.41)	0.68 (0.59-0.75)	500 (>37.8)	0.02 (<0.03)	1.66 (1.61-1.71)	1197.5/971 (>99.9%)
	S0-3, PSPC <sup>b</sup>	3.87 (3.32-4.50)	0.77 (0.70-0.82)	5.9 (4.3-8.1)	1.05 (0.79-1.33)	2.12 (1.96-2.29)	925.1/835 (98.4%)
NGC 3079	S0-3	61.3 (8.72-98.4)	0.14 (<0.54)	1.2 (<12.9)	0.05 (<4.41)	2.20 (1.24-4.24)	251.9/229 (85.7%)
	S0-3, PSPC <sup>a</sup>	0.00 (<6.75)	0.35 (0.26-0.80)	71.9 (>4.6)	0.08 (<7.17)	2.03 (1.16-2.58)	366.8/301 (99.4%)
	S0-3, PSPC <sup>b</sup>	0.49 (<8.63)	0.35 (0.27-0.72)	225 (>11.9)	0.08 (<0.41)	2.06 (1.08-2.58)	299.8/263 (94.1%)
NGC 3147	S0-3	0.00 (<9.32)	2.63 (0.50-5.60)	4.0 (<50.4)	2.04 (<385.00)	0.23 (-2.34-1.71)	344.5/353 (38.3%)
	S0-3, PSPC <sup>a</sup>	1.34 (0.79-2.18)	1.64 (0.46-3.31)	0.0 (<12.4)	1.44 (<11.90)	0.88 (-0.54-1.75)	391.5/416 (19.9%)
	S0-3, PSPC <sup>b</sup>	1.57 (1.02-2.41)	1.40 (<2.89)	0.0 (<8.0)	1.18 (<7.48)	1.04 (-0.25-1.76)	387.7/402 (31.3%)
NGC 3310 Obs. 1	S0-3	17.7 (<36.4)	0.78 (<1.01)	3.2	2.93 (<6.10)	2.35 (1.50-3.45)	204.5/189 (79.1%)
	S0-3, PSPC <sup>a</sup>	76.3 (4.2-110.)	0.14 (<0.87)	2.2 (<54.4)	0.28 (<4.86)	2.13 (1.67-3.20)	270.6/242 (90.0%)
	S0-3, PSPC <sup>b</sup>	5.60 (3.46-11.5)	0.81 (0.62-0.96)	5.8 (1.7-14.2)	1.75 (0.29-4.26)	2.08 (1.47-2.99)	250.9/220 (92.5%)
NGC 3628	S0-3	88.6 (<133.)	0.11 (<1.69)	500	0.12 (<1.18)	1.73 (1.23-2.38)	62.7/73 (20.0%)
	S0-3, PSPC <sup>a</sup>	3.29 (0.83-9.79)	0.90	3.6 (<41.0)	1.17 (0.17-4.47)	1.74 (1.04-2.35)	144.2/135 (72.2%)
	S0-3, PSPC <sup>b</sup>	6.26 (<143.)	0.90	11.5	0.99 (<22.90)	1.74 (0.59-2.32)	124.3/108 (86.5%)
NGC 3998	S0-3	5.53 (<11.9)	0.94 (0.57-2.36)	0.8 (<3.2)	0.63 (<1.37)	1.71 (0.93-1.91)	805.9/832 (26.4%)
	S0-3, PSPC <sup>a</sup>	2.82 (2.43-3.19)	0.24 (0.19-0.28)	2.1 (1.2-3.3)	0.19 (0.12-0.25)	1.96 (1.89-2.03)	1291.4/1028 (>99.9%)
	S0-3, PSPC <sup>b</sup>	3.19 (2.88-3.48)	0.25 (0.22-0.35)	1.5 (0.7-2.5)	0.21 (0.15-0.33)	1.97 (1.90-2.04)	1397.2/1028 (>99.9%)
NGC 4258	S0-3	3.47 (0.84-6.37)	0.66 (0.61-0.69)	6.5 (5.1-8.2)	6.62 (5.16-8.32)	1.14 (0.89-1.41)	827.9/666 (>99.9%)
	S0-3, PSPC <sup>a</sup>	1.78 (1.52-2.07)	0.62 (0.59-0.65)	5.9 (4.8-7.2)	5.76 (4.42-7.35)	1.05 (0.81-1.32)	1190.4/886 (>99.9%)
	S0-3, PSPC <sup>b</sup>	1.70 (1.46-1.97)	0.63 (0.60-0.66)	6.1 (5.0-7.5)	6.08 (4.73-7.69)	1.09 (0.85-1.36)	1105.3/815 (>99.9%)
NGC 4579	S0-3	3.62 (<14.8)	0.86 (0.75-1.07)	4.2 (0.9-13.3)	0.47 (<2.46)	1.59 (1.38-1.79)	587.5/595 (42.1%)
	S0-3, PSPC <sup>a</sup>	2.57 (2.21-2.94)	0.84 (0.71-0.99)	3.2 (1.6-5.0)	0.69 (0.30-1.10)	1.65 (1.46-1.85)	839.2/753 (98.5%)
	S0-3, PSPC <sup>b</sup>	3.12 (2.79-3.46)	0.86 (0.71-1.02)	2.9 (1.5-4.5)	0.79 (0.40-1.30)	1.65 (1.45-1.85)	873.4/746 (>99.9%)
NGC 4594	S0-3	0.00 (<49.8)	0.78 (0.22-0.93)	9.0 (<21.6)	0.79 (0.27-3.35)	1.94 (1.67-2.72)	242.9/279 (5.8%)
	S0-3, PSPC <sup>a</sup>	4.53 (3.15-6.70)	0.76 (0.47-0.88)	4.7 (1.9-9.6)	1.03 (0.37-1.77)	1.97 (1.68-2.30)	338.2/365 (16.0%)
	S0-3, PSPC <sup>b</sup>	4.39 (2.96-6.19)	0.67 (0.45-0.87)	4.4 (2.1-9.3)	0.85 (0.36-1.64)	1.97 (1.70-2.30)	286.4/323 (7.1%)
NGC 6946	S0-3	16.3 (10.3-26.6)	0.98 (0.63-1.16)	3.6 (0.4-9.1)	5.70 (<21.7)	2.53 (1.25-5.13)	268.2/257 (69.7%)
	S0-3, PSPC <sup>a</sup>	15.2 (1.18-23.2)	0.83 (0.67-0.98)	10.8 (>2.1)	0.01 (<0.22)	2.15 (1.33-2.65)	437.4/406 (86.4%)
	S0-3, PSPC <sup>b</sup>	18.9 (12.7-25.7)	0.86 (0.66-1.08)	2.7 (0.7-7.7)	4.60 (<11.80)	2.53 (1.44-4.11)	371.5/357 (71.2%)
M51 PV Obs.	S0-3	16.7 (8.57-27.0)	0.32 (0.25-0.41)	2.3 (1.4-4.7)	1.14 (<2.64)	1.90 (1.21-2.61)	439.8/325 (>99.9%)
	S0-3, PSPC <sup>a</sup>	2.33 (1.94-2.68)	0.52 (0.39-0.60)	3.0 (2.3-4.7)	1.69 (<3.54)	1.74 (1.02-2.47)	616.6/465 (>99.9%)
	S0-3, PSPC <sup>b</sup>	1.97 (1.64-2.33)	0.51 (0.37-0.56)	3.3 (2.6-7.2)	1.99 (<3.86)	1.84 (1.08-2.58)	579.3/422 (>99.9%)
M82	S0-3	16.0 (10.9-19.8)	0.79 (0.75-0.81)	6.6 (4.9-9.6)	1.17 (0.73-1.63)	1.64 (1.55-1.75)	1650.7/1156 (>99.9%)
	S0-3, PSPC <sup>a</sup>	9.92 (8.44-12.3)	0.74 (0.69-0.77)	7.2 (5.6-8.8)	0.85 (0.66-1.08)	1.66 (1.59-1.74)	2552.5/1710 (>99.9%)
	S0-3, PSPC <sup>b</sup>	20.0 (15.0-23.7)	0.75 (0.72-0.78)	7.3 (5.4-10.5)	0.92 (0.56-1.31)	1.64 (1.56-1.73)	2434.9/1618 (>99.9%)

<sup>a</sup>PSPC source region size = *ASCA* SIS source region size

<sup>b</sup>PSPC source region size = 1.25'



TABLE 9  
RATIO OF *ASCA* AND *ROSAT* PSPC FLUXES

Galaxy	Det.	S0*	S1/S0	G2/S0	G3/S0	PSPC/S0		
NGC 253	S0-3	3.183	0.93	1.08	1.04	...	...	...
	S0-3, PSPC <sup>a</sup>	3.274	0.93	1.10	1.06	0.98	0.95	...
	S0-3, PSPC <sup>b</sup>	3.173	0.93	1.08	1.04	0.53	0.51	...
NGC 3079	S0-3	0.468	0.94	0.91	1.02	...	...	...
	S0-3, PSPC <sup>a</sup>	0.456	0.94	0.93	1.02	0.88	...	...
	S0-3, PSPC <sup>b</sup>	0.450	0.95	0.91	1.01	0.72	...	...
NGC 3147	S0-3	0.860	1.18	1.05	1.18	...	...	...
	S0-3, PSPC <sup>a</sup>	0.869	1.18	1.06	1.19	1.21	...	...
	S0-3, PSPC <sup>b</sup>	0.871	1.18	1.06	1.19	1.10	...	...
NGC 3310 Obs.1	S0-3	0.870	1.07	0.96	1.01	...	...	...
	S0-3, PSPC <sup>a</sup>	0.919	1.06	0.98	1.04	0.80	...	...
	S0-3, PSPC <sup>b</sup>	0.908	1.06	0.97	1.03	0.87	...	...
NGC 3628	S0-3	0.208	1.10	0.92	1.19	...	...	...
	S0-3, PSPC <sup>a</sup>	0.170	1.13	0.91	1.16	4.04	...	...
	S0-3, PSPC <sup>b</sup>	0.155	1.14	0.92	1.16	3.88	...	...
NGC 3998	S0-3	4.614	1.04	0.98	0.99	...	...	...
	S0-3, PSPC <sup>a</sup>	4.779	1.04	1.01	1.02	1.07	...	...
	S0-3, PSPC <sup>b</sup>	4.757	1.04	1.01	1.03	1.05	...	...
NGC 4258	S0-3	1.788	0.96	1.01	1.12	...	...	...
	S0-3, PSPC <sup>a</sup>	1.826	0.96	1.03	1.14	1.08	1.10	...
	S0-3, PSPC <sup>b</sup>	1.822	0.96	1.03	1.14	0.58	0.57	...
NGC 4579	S0-3	2.344	0.98	0.94	1.02	...	...	...
	S0-3, PSPC <sup>a</sup>	2.384	0.98	0.95	1.03	2.28	...	...
	S0-3, PSPC <sup>b</sup>	2.391	0.98	0.96	1.03	2.23	...	...
NGC 4594	S0-3	1.069	1.00	1.22	1.07	...	...	...
	S0-3, PSPC <sup>a</sup>	1.089	1.01	1.23	1.09	1.50	...	...
	S0-3, PSPC <sup>b</sup>	1.085	1.00	1.23	1.08	0.86	...	...
NGC 6946	S0-3	1.088	1.01	1.10	1.15	...	...	...
	S0-3, PSPC <sup>a</sup>	1.100	1.00	1.11	1.16	1.14	...	...
	S0-3, PSPC <sup>b</sup>	1.090	1.01	1.11	1.16	0.74	...	...
M51 PV Obs.	S0-3	1.606	1.05	1.13	1.21	...	...	...
	S0-3, PSPC <sup>a</sup>	1.555	1.05	1.11	1.19	1.19	...	...
	S0-3, PSPC <sup>b</sup>	1.565	1.05	1.15	1.24	0.50	...	...
M82	S0-3	9.595	1.02	1.13	1.13	...	...	...
	S0-3, PSPC <sup>a</sup>	9.713	1.02	1.14	1.14	1.23	1.22	0.87
	S0-3, PSPC <sup>b</sup>	9.369	1.02	1.12	1.12	0.95	0.94	0.60

\*0.5-2.0 keV flux observed with the *ASCA* SIS0 detector, in units of  $10^{-12}$  ergs  $\text{cm}^{-2}$   $\text{s}^{-1}$

<sup>a</sup>PSPC source region size = *ASCA* source region size

<sup>b</sup>PSPC source region size = 1.25'

TABLE 10  
 FE-K LINE EMISSION DETECTIONS AND UPPER-LIMITS

Galaxy	$N_H$ ( $10^{22}$ cm $^{-2}$ )	$\Gamma$	E (keV)	$\sigma$ (keV)	Norm.**	EW (keV)	$\chi^2/\text{dof}$
NGC 253	0.0 (<3)	2.0 (1.8-2.5)	6.4*	0.01*	0.468 (<1.23)	0.091 (<0.24)	403.5/433
	0.0 (<3.1)	2.0 (1.8-2.5)	6.4*	0.1*	0.658 (<1.55)	0.13 (<0.3)	402.4/433
	0.0 (<3.4)	2.0 (1.8-2.6)	6.4*	0.5*	1.01 (<2.9)	0.2 (<0.58)	403.9/433
	0.0 (<3)	2.0 (1.8-2.5)	6.7*	0.01*	0.333 (<1.09)	0.07 (<0.23)	404.6/433
	0.0 (<3.1)	2.0 (1.8-2.5)	6.7*	0.1*	0.391 (<1.29)	0.083 (<0.27)	404.6/433
	0.0 (<3.1)	1.9 (1.7-2.5)	6.7*	0.5*	0.241 (<2.13)	0.051 (<0.45)	405.7/433
NGC 3079	0.0 (<36)	2.1 (>0.39)	6.4*	0.01*	0.349 (<1.17)	1.3 (<4.4)	125.7/142
	0.0 (<40)	2.2 (>0.47)	6.4*	0.1*	0.467 (<1.6)	1.9 (<6.4)	124.1/142
	4.5 (<45)	3.8 (>0.86)	6.4*	0.5*	1.11 (0.0394-4.36)	7.5 (0.26-29)	122.3/142
	0.0 (<31)	2.0 (0.31-8.8)	6.7*	0.01*	0.219 (<0.799)	0.85 (<3.1)	127.4/142
	0.0 (<33)	2.0 (0.35-9.4)	6.7*	0.1*	0.295 (<1.01)	1.2 (<4.1)	126.7/142
	0.0 (<43)	2.5 (>0.59)	6.7*	0.5*	0.788 (<3.39)	4.1 (<18)	125.3/142
NGC 3147	0 (<29)	1.8 (1.3-8.5)	6.6 (>6.3)	0.23	1.13 (0.252-238)	0.8 (0.18-170)	202.2/207
	0 (<4.3)	1.7 (1.3-2.5)	6.5 (6.3-6.8)	0.01*	0.787 (0.236-206)	0.5 (0.15-130)	203.9/208
	0 (<4.7)	1.7 (1.3-2.5)	6.5 (6.3-6.8)	0.1*	0.893 (0.282-218)	0.59 (0.19-140)	203.0/208
	0 (<10)	1.9 (1.4-3.9)	6.8 (6.4-7.2)	0.5*	1.69 (0.549-215)	1.4 (0.44-170)	202.8/208
	0 (<4.2)	1.7 (1.3-2.4)	6.4*	0.0 (<0.76)	0.717 (0.175-205)	0.45 (0.11-130)	206.1/208
	0 (<3.5)	1.7 (1.3-2.3)	6.4*	0.01*	0.709 (0.224-185)	0.44 (0.14-120)	206.3/209
	0 (<3.6)	1.7 (1.3-2.4)	6.4*	0.1*	0.77 (0.235-184)	0.48 (0.15-.20)	206.7/209
	0 (<5.2)	1.9 (1.4-3)	6.4*	0.5*	1.25 (0.235-182)	0.87 (0.16-130)	210.4/209
	0 (<14)	1.9 (1.4-4.3)	6.7*	0.38	1.42 (0.389-201)	1.1 (0.29-150)	202.3/208
	0 (<3.8)	1.7 (1.3-2.3)	6.7*	0.01*	0.624 (0.127-179)	0.42 (0.085-120)	209.9/209
	0 (<4)	1.7 (1.3-2.4)	6.7*	0.1*	0.762 (0.218-179)	0.52 (0.15-120)	207.6/209
	0 (<8.3)	2.0 (1.5-3.6)	6.7*	0.5*	1.69 (0.655-180)	1.3 (0.52-140)	203.0/209
	NGC 3310	1.1 (<17)	2.4 (1.6-5.2)	6.4*	0.01*	0.166 (<1.18)	0.12 (<0.87)
1.1 (<17)		2.4 (1.6-5.3)	6.4*	0.1*	0.162 (<1.29)	0.12 (<0.95)	110.9/103
1.3 (<22)		2.5 (1.6-6.6)	6.4*	0.5*	0.251 (<2.87)	0.19 (<2.1)	111.0/103
0.82 (<16)		2.3 (1.6-5.1)	6.7*	0.01*	0.0655 (<1.07)	0.053 (<0.86)	111.1/103
0.97 (<17)		2.4 (1.6-5.2)	6.7*	0.1*	0.103 (<1.19)	0.083 (<0.96)	111.0/103
2.4 (<23)		2.7 (1.6-6.7)	6.7*	0.5*	0.496 (<3.09)	0.43 (<2.7)	110.7/103
NGC 3628	0.0 (<14)	1.6 (0.97-3.8)	6.4*	0.01*	0 (<0.43)	0.0 (<0.50)	27.9/50
	0 (<14)	1.6 (0.97-3.9)	6.4*	0.1*	0 (<0.46)	0.0 (<0.55)	27.9/50
	0.0 (<15)	1.6 (0.97-4.1)	6.4*	0.5*	0 (<0.877)	0 (0-1.2)	27.9/50
	0.0 (<15)	1.6 (0.96-4)	6.7*	0.01*	0 (<0.576)	0 (0-0.76)	27.9/50
	0.0 (<15)	1.6 (0.96-4)	6.7*	0.1*	0 (<0.611)	0 (0-0.82)	27.9/50
	0.0 (<16)	1.6 (0.96-4.3)	6.7*	0.5*	0 (<1.03)	0 (0-1.6)	27.9/50
NGC 3998	0.0 (<2)	1.9 (1.7-2.2)	6.4*	0.01*	0.659 (<1.43)	0.087 (<0.19)	542.7/577
	0.0 (<2)	1.9 (1.7-2.2)	6.4*	0.1*	0.806 (<1.7)	0.11 (<0.22)	542.2/577
	0.0 (<2.2)	1.9 (1.7-2.3)	6.4*	0.5*	1.14 (<3.01)	0.15 (<0.4)	544.9/577
	0.0 (<1.9)	1.9 (1.7-2.2)	6.7*	0.01*	0.301 (<1.09)	0.042 (<0.15)	546.4/577
	0.0 (<2)	1.9 (1.7-2.2)	6.7*	0.1*	0.394 (<1.3)	0.056 (<0.18)	546.1/577
	0.0 (<2.4)	1.9 (1.7-2.3)	6.7*	0.5*	0.979 (<2.91)	0.14 (<0.42)	545.5/577
NGC 4258	10 (6.9-13)	1.6 (1.2-2)	6.8 (5.7-7)	0	1.22 (0.205-2.26)	0.13 (0.02-0.24)	645.6/654
	10 (7.2-13)	1.6 (1.3-2)	6.8 (6.7-6.9)	0.01*	1.24 (0.302-2.2)	0.13 (0.03-0.23)	645.5/655
	10 (7.2-13)	1.6 (1.3-2)	6.8 (6.6-7)	0.1*	1.28 (0.211-2.37)	0.14 (0.02-0.25)	647.9/655
	9.7 (6.6-13)	1.6 (1.2-2)	6.5	0.5*	1.82 (<3.95)	0.18 (<0.4)	653.1/655
	9.6 (6.4-13)	1.6 (1.2-2)	6.4*	0.49	1.77 (<7.37)	0.17 (<0.72)	653.3/655
	9.8 (7.3-13)	1.6 (1.2-1.9)	6.4*	0.01*	0.335 (<1.07)	0.032 (<0.1)	657.6/656
	9.8 (7.2-13)	1.6 (1.3-1.9)	6.4*	0.1*	0.529 (<1.42)	0.05 (<0.14)	656.7/656
	9.6 (6.9-12)	1.6 (1.3-1.9)	6.4*	0.5*	1.78 (<3.65)	0.17 (<0.36)	653.3/656
	10 (7.1-13)	1.6 (1.3-2)	6.7*	0.17	1.18 (<5.96)	0.12 (<0.62)	651.4/655
	9.9 (7.3-13)	1.6 (1.3-1.9)	6.7*	0.01*	0.702 (<1.47)	0.072 (<0.15)	653.6/656
	9.9 (7.4-13)	1.6 (1.3-1.9)	6.7*	0.1*	0.956 (0.0435-1.87)	0.10 (0.01-0.19)	652.0/656
	10 (7.4-13)	1.6 (1.3-2)	6.7*	0.5*	1.72 (<3.68)	0.18 (<0.39)	653.9/656

TABLE 10—*Continued*

Galaxy	$N_H$ ( $10^{22}$ cm $^{-2}$ )	$\Gamma$	E (keV)	$\sigma$ (keV)	Norm.**	EW (keV)	$\chi^2/\text{dof}$	
NGC 4579	0.22 (<6.3)	1.9 (1.6-3.4)	6.7 (5.9-7.1)	0.31	1.91 (0.292-7.98)	0.53 (0.082-2.2)	371.5/384	
	0 (<4.1)	1.8 (1.6-2.5)	6.5 (6.3-7.2)	0.01*	0.965 (0.112-1.84)	0.25 (0.029-0.47)	375.8/385	
	0 (<4.3)	1.8 (1.6-2.5)	6.6 (6.3-7.2)	0.1*	1.1 (0.16-2.08)	0.29 (0.042-0.54)	375.1/385	
	0.52 (<6.3)	2 (1.6-3)	6.7 (6.2-7.1)	0.5*	2.41 (0.504-4.67)	0.7 (0.15-1.3)	373.2/385	
	0 (<4.5)	2 (1.6-2.8)	6.4*	0.62	2.37 (0.124-6.51)	0.64 (0.034-1.8)	376.2/385	
	0.0 (<3.4)	1.8 (1.6-2.3)	6.4*	0.01*	0.719 (<1.46)	0.18 (<0.36)	379.8/386	
	0.0 (<3.5)	1.8 (1.6-2.4)	6.4*	0.1*	0.83 (0.0199-1.65)	0.2 (0.0049-0.41)	379.2/386	
	0 (<4.4)	1.9 (1.6-2.7)	6.4*	0.5*	1.95 (0.365-3.67)	0.51 (0.096-0.97)	376.3/386	
	0.16 (<5.7)	1.9 (1.6-3.1)	6.7*	0.31	1.9 (0.427-6.01)	0.53 (0.12-1.7)	371.5/385	
	0 (<3.6)	1.8 (1.6-2.4)	6.7*	0.01*	0.833 (0.0722-110)	0.22 (0.019-29)	378.2/386	
	0 (>3.9)	1.8 (1.6-2.4)	6.7*	0.1*	1.07 (0.215-1.95)	0.28 (0.057-0.52)	375.9/386	
	0.59 (<5.7)	2 (1.7-2.9)	6.7*	0.5*	2.43 (0.691-4.43)	0.7 (0.2-1.3)	373.3/386	
	NGC 4594	5.7 (<14)	2.8 (1.7-4.2)	6.4*	0.01*	0.0 (<0.746)	0.0 (0-0.33)	146.7/159
		5.7 (<14)	2.8 (1.7-4.2)	6.4*	0.1*	0.0 (<0.813)	0.0 (0-0.36)	146.7/159
5.8 (<16)		2.8 (1.7-4.8)	6.4*	0.5*	0.0338 (<2.12)	0.014 (<0.88)	146.7/159	
5.7 (<14)		2.8 (1.7-4.2)	6.7*	0.01*	0.0 (<0.835)	0.0 (<0.39)	146.7/159	
5.8 (<14)		2.8 (1.7-4.3)	6.7*	0.1*	0.00882 (<0.923)	0.0041 (<0.43)	146.7/159	
6.5 (<17)		2.9 (1.7-5)	6.7*	0.5*	0.284 (<2.44)	0.14 (<1.2)	146.6/159	
NGC 6946	6.3 (<24)	3.5 (1.9-6.9)	6.4*	0.01*	0.0436 (<0.674)	0.063 (<0.97)	121.3/112	
	6.5 (<24)	3.6 (1.9-7)	6.4*	0.1*	0.0595 (<0.766)	0.086 (<1.1)	121.2/112	
	9.3 (<32)	4.3 (2-8.9)	6.4*	0.5*	0.441 (<2.18)	0.72 (<3.6)	120.6/112	
	8.2 (<27)	4 (2-7.5)	6.7*	0.01*	0.267 (<1.07)	0.48 (<1.9)	120.3/112	
	8.4 (<27)	4 (2-7.6)	6.7*	0.1*	0.294 (<1.15)	0.54 (<2.1)	120.2/112	
	9.7 (<31)	4.3 (2-8.5)	6.7*	0.5*	0.493 (<2.1)	0.96 (<4.1)	120.4/112	
M51	4.6 (<24)	2.4 (>1)	6.3 (6-6.9)	0.14	0.864 (0.165-9.66)	1 (0.2-12)	190.7/176	
	3.9 (<19)	2.2 (1.1-4.8)	6.3 (6.1-6.5)	0.01*	0.691 (0.195-1.35)	0.79 (0.22-1.5)	191.0/177	
	4.4 (<20)	2.4 (1.1-5.2)	6.3 (6.1-6.5)	0.1*	0.803 (0.216-1.6)	0.95 (0.26-1.9)	190.8/177	
	7.5 (<33)	3.2 (1.2-8.8)	6.3 (5.7-6.9)	0.5*	1.47 (0.222-4.03)	2.1 (0.32-5.9)	194.7/177	
	5.2 (<37)	2.5 (1.1-8.6)	6.4*	0.12	0.8 (0.164-6.05)	0.99 (0.2-7.5)	192.4/177	
	4.8 (<18)	2.3 (1.1-4.6)	6.4*	0.01*	0.666 (0.196-1.25)	0.79 (0.23-1.5)	193.1/178	
	5.1 (<19)	2.4 (1.2-4.9)	6.4*	0.1*	0.775 (0.238-1.48)	0.95 (0.29-1.8)	192.5/178	
	7.6 (<28)	3.2 (1.3-7.2)	6.4*	0.5*	1.45 (0.322-3.28)	2.2 (0.48-4.9)	194.9/178	
	11 (<26)	4 (1.2-6.2)	6.7*	0.91 (>0.05)	2.4 (0.0623-4.99)	5 (0.13-10)	197.4/177	
	3.9 (<16)	2 (0.94-3.9)	6.7*	0.01*	0.147 (<0.615)	0.17 (<0.72)	205.2/178	
	4.1 (<16)	2 (0.95-4)	6.7*	0.1*	0.182 (<0.691)	0.21 (<0.81)	205.0/178	
	7 (<23)	2.9 (1.2-5.9)	6.7*	0.5*	1.09 (0.0348-2.5)	1.6 (0.051-3.6)	199.2/178	
	M82	2.7 (0.74-4.9)	2.1 (1.8-2.6)	6.8 (6.3-7.2)	0.49 (>0.13)	6.09 (1.79-18.3)	0.32 (0.094-0.96)	812.9/903
2.2 (0.6-3.9)		1.9 (1.7-2.2)	6.9 (6.2-7.2)	0.01*	1.69 (0.2-3.2)	0.087 (0.01-0.16)	827.0/904	
2.2 (0.61-4)		2 (1.7-2.2)	6.8 (6.2-7.1)	0.1*	2.25 (0.524-4.01)	0.11 (0.027-0.2)	823.7/904	
2.7 (0.94-4.6)		2.1 (1.8-2.4)	6.8 (6.5-7.2)	0.5*	6.21 (2.65-9.91)	0.33 (0.14-0.52)	812.9/904	
2.1 (0.4-2.7)		2.1 (1.8-2.2)	6.4*	1 (>0.081)	9.98 (1.27-14.2)	0.48 (0.061-0.69)	820.3/904	
2 (0.59-3.5)		1.9 (1.7-2.1)	6.4*	0.01*	1.29 (0.0602-2.53)	0.057 (0.0027-0.11)	830.1/905	
2 (0.59-3.5)		1.9 (1.7-2.1)	6.4*	0.1*	1.79 (0.334-3.25)	0.08 (0.015-0.14)	827.6/905	
2.1 (0.59-3.6)		2 (1.8-2.2)	6.4*	0.5*	4.5 (1.51-7.52)	0.21 (0.069-0.34)	822.9/905	
2.5 (0.81-4.3)		2 (1.8-2.4)	6.7*	0.47 (>0.15)	5.68 (1.91-16.9)	0.28 (0.096-0.85)	813.8/904	
2.1 (0.69-3.6)		1.9 (1.7-2.1)	6.7*	0.01*	1.55 (0.277-2.83)	0.075 (0.013-0.14)	827.7/905	
2.2 (0.73-3.7)		1.9 (1.7-2.2)	6.7*	0.1*	2.16 (0.654-3.68)	0.1 (0.032-0.18)	824.1/905	
2.5 (1-4.1)		2.1 (1.8-2.3)	6.7*	0.5*	5.99 (2.86-9.2)	0.3 (0.14-0.46)	813.8/905	

\*Parameter fixed at this value

\*\*Line normalization in units of  $10^{-5}$  photons s $^{-1}$  cm $^{-2}$

TABLE 12  
FLUXES AND LUMINOSITIES

Galaxy (1)	Dets. (2)	Model (3)	Total (4)	RS Obs. (5)	PL Obs. (6)	RS Int. (7)	PL Int. (8)	RS/PL Obs. (9)	RS/PL Int. (10)	Lum. Total (11)
M51	S0-3	RSPL	2.95	1.82	1.13	4.34	2.07	161%	210%	7.35
PV Obs.	S0-3, PSPC <sup>a</sup>	RSPL	2.97	1.90	1.07	2.12	1.88	177%	113%	7.41
M51	S0-3	RSPL	2.58	1.48	1.10	1.81	2.21	135%	82%	6.42
AO Obs.										
M82	S0-3	RSPL	33.1	9.89	23.21	16.6	36.69	43%	45%	5.45
	S0-3, PSPC <sup>a</sup>	RSPL	33.3	8.89	24.4	12.6	36.7	36%	34%	5.49
NGC 253	S0-3	RSPL	8.82	2.85	5.97	3.65	12.7	48%	29%	0.70
	S0-3, PSPC <sup>a</sup>	RSPL	9.60	0.47	9.13	0.47	9.41	5%	5%	0.76
NGC 3079	S0-3	RSPL	0.87	0.34	0.53	18.3	1.01	65%	1805%	9.21
	S0-3, PSPC <sup>a</sup>	RSPL	0.86	0.17	0.69	0.17	0.79	25%	22%	9.09
NGC 3147	S0-3	RSPL	2.95	1.80	1.15	1.80	1.30	157%	138%	119.
	S0-3, PSPC <sup>a</sup>	RSPL	2.92	1.45	1.47	1.50	1.79	98%	84%	118.
	S0-3, PSPC <sup>a</sup>	PL	2.69	...	2.69	...	2.76	...	...	109.
NGC 3310	S0-3	RSPL	2.53	0.96	1.57	1.71	5.43	61%	32%	12.1
Obs. 1	S0-3, PSPC <sup>a</sup>	RSPL	2.61	0.62	1.99	58.1	4.04	31%	1437%	12.5
	S0-3, PSPC <sup>b</sup>	RSPL	2.65	0.91	1.74	1.12	3.92	52%	28%	12.7
NGC 3310	S0-3	RSPL	2.93	0.67	2.26	1.15	3.09	30%	37%	14.0
Obs. 2										
NGC 3310	S0-3	RSPL	2.45	0.43	2.02	69.5	4.29	21%	1619%	11.7
Obs. 3										
NGC 3628	S0-3	RSPL	1.10	0.10	1.00	45.9	1.57	10%	2920%	3.11
	S0-3, PSPC <sup>a</sup>	RSPL	1.07	0.10	0.97	0.11	1.59	10%	7%	3.02
NGC 3998	S0-3	RSPL	13.2	4.33	8.81	5.27	12.8	49%	41%	98.7
	S0-3, PSPC <sup>a</sup>	RSPL	13.2	1.43	11.8	1.72	15.5	12%	11%	99.0
NGC 4258	S0-3	RSPL	8.54	2.09	6.45	2.40	11.1	32%	22%	11.3
	S0-3, PSPC <sup>a</sup>	RSPL	8.72	1.69	7.03	1.69	7.74	24%	22%	11.5
NGC 4579	S0-3	RSPL	6.82	1.92	4.89	2.19	6.48	39%	34%	113.
	S0-3, PSPC <sup>a</sup>	RSPL	6.87	2.16	4.71	2.38	6.77	46%	35%	114.
NGC 4594	S0-3	RSPL	3.7	0.76	2.94	0.76	4.94	26%	15%	24.
	S0-3, PSPC <sup>a</sup>	RSPL	3.73	0.94	2.79	1.11	5.12	34%	22%	24.2
NGC 6946	S0-3	RSPL	2.24	1.53	0.72	2.45	3.98	212%	62%	1.96
	S0-3, PSPC <sup>a</sup>	RSPL	2.28	0.6	1.69	0.96	2.24	35%	43%	2.00

s in Table 8.

NOTE.—(3) PL = power-law fit, RSPL = Raymond-Smith plus power-law fit; (4) Total observed flux; (5) Observed flux of Raymond-Smith component only; (6) Observed flux of power-law component only; (7) Absorption-corrected flux of the Raymond-Smith component; (8) Absorption-corrected flux of the power-law component; (9) Ratio of the observed Raymond-Smith and power-law fluxes; (10) Ratio of the absorption-corrected Raymond-Smith and power-law fluxes; The fluxes in columns 4-8 are in the 0.4-10.0 keV bandpass, in units of  $10^{-12}$  ergs  $s^{-1}$   $cm^{-2}$ ; the luminosity in column 11 is in the 0.4-10.0 keV bandpass, in units of  $10^{40}$  ergs  $s^{-1}$ .

<sup>a, b</sup>A

TABLE 13  
DOUBLE RAYMOND-SMITH PLUS POWER-LAW FITS

Fit Parameter	<i>ASCA</i> + PSPC, SIS 0.4-10.0 keV	<i>ASCA</i> + PSPC, SIS 0.6-10.0 keV
NGC 253		
$N_H$ ( $10^{20}$ cm $^{-2}$ )	1.9 (1.1-3.1)	2.3 (1.6-3.0)
kT <sub>1</sub> (keV)	0.33 (0.18-0.68)	0.69 (0.20-0.84)
$A_1$ ( $/A_\odot$ )	0.10 (0.03-0.38)	0.11 (<0.29)
$A_{1,Fe}$ ( $/A_{\odot,Fe}$ )	0.046 (0.003-0.262)	0.025 (0.012-0.047)
$N_{H,2}$ ( $10^{21}$ cm $^{-2}$ )	7.2 (1.8-26.1)	14.5 (0.9-32.3)
kT <sub>2</sub> (keV)	0.72 (0.59-1.59)	0.96 (0.27-2.17)
$A_2$ ( $/A_\odot$ )	0.39 (>0.03)	0.21 (>0.02)
$A_{2,Fe}$ ( $/A_{\odot,Fe}$ )	0.22 (>0.03)	0.00
$N_{H,3}$ ( $10^{22}$ cm $^{-2}$ )	1.6 (0.6-12.2)	4.0 (<23.1)
$\Gamma$	2.03 (1.61-2.46)	1.92 (1.08-3.10)
$\chi^2/\text{dof}$	970.8/965 (55.8%)	925.8/949 (30.1%)
NGC 4258		
$N_H$ ( $10^{20}$ cm $^{-2}$ )	1.6 (0.8-2.6)	1.9 (<3.7)
kT <sub>1</sub> (keV)	0.25 (0.19-0.36)	0.25 (0.17-0.39)
$A_1$ ( $/A_\odot$ )	0.13 (0.05-0.38)	0.19 (>0.01)
$A_{1,Fe}$ ( $/A_{\odot,Fe}$ )	0.19 (0.08-0.94)	0.34 (>0.03)
$N_{H,2}$ ( $10^{21}$ cm $^{-2}$ )	3.6 (1.0-7.6)	0.0 (<7.7)
kT <sub>2</sub> (keV)	0.73 (0.66-0.83)	0.74 (0.64-0.87)
$A_2$ ( $/A_\odot$ )	0.20 (0.03-0.64)	0.13 (0.01-0.67)
$A_{2,Fe}$ ( $/A_{\odot,Fe}$ )	0.19 (0.07-0.55)	0.06 (0.03-0.49)
$N_{H,3}$ ( $10^{22}$ cm $^{-2}$ )	7.8 (5.4-10.6)	6.9 (4.7-9.6)
$\Gamma$	1.26 (0.90-1.66)	1.18 (0.83-1.57)
$\chi^2/\text{dof}$	1038.4/880 (>99.9%)	1004.6/864 (>99.9%)
M51 (PV Obs.)		
$N_H$ ( $10^{20}$ cm $^{-2}$ )	2.2 (<3.1)	2.5 (<4.4)
kT <sub>1</sub> (keV)	0.35 (>0.15)	0.35 (<2.0)
$A_1$ ( $/A_\odot$ )	0.07	0.04 (<1.02)
$A_{1,Fe}$ ( $/A_{\odot,Fe}$ )	0.04	0.03 (<0.19)
$N_{H,2}$ ( $10^{21}$ cm $^{-2}$ )	0.0	0.0 (<1.5)
kT <sub>2</sub> (keV)	0.72 (>0.16)	0.71 (>0.43)
$A_2$ ( $/A_\odot$ )	0.25	0.25
$A_{2,Fe}$ ( $/A_{\odot,Fe}$ )	0.11	0.10
$N_{H,3}$ ( $10^{22}$ cm $^{-2}$ )	0.4 (<5.1)	0.8 (<4.8)
$\Gamma$	1.47 (0.71-2.56)	1.55 (0.75-2.52)
$\chi^2/\text{dof}$	568.5/459 (>99.9%)	544.2/444 (>99.9%)
M82		
$N_H$ ( $10^{20}$ cm $^{-2}$ )	7.6 (5.2-10.8)	7.4 (3.3-11.1)
kT <sub>1</sub> (keV)	0.35 (0.27-0.48)	0.35 (0.25-0.48)
$A_1$ ( $/A_\odot$ )	0.19 (0.07-0.68)	0.22 (>0.06)
$A_{1,Fe}$ ( $/A_{\odot,Fe}$ )	0.11 (0.05-0.33)	0.12 (>0.04)
$N_{H,2}$ ( $10^{21}$ cm $^{-2}$ )	5.3 (3.0-8.1)	5.4 (3.1-8.1)
kT <sub>2</sub> (keV)	0.72 (0.64-0.82)	0.72 (0.64-0.82)
$A_2$ ( $/A_\odot$ )	0.42 (0.27-1.33)	0.41 (0.26-1.58)
$A_{2,Fe}$ ( $/A_{\odot,Fe}$ )	0.12 (0.05-0.44)	0.12 (0.05-0.50)
$N_{H,3}$ ( $10^{22}$ cm $^{-2}$ )	2.3 (1.1-3.6)	2.4 (1.1-3.7)
$\Gamma$	1.76 (1.57-1.95)	1.76 (1.57-1.95)
$\chi^2/\text{dof}$	2039.9/1699 (>99.9%)	2032.8/1692 (>99.9%)

NOTE.—Fits are to all *ASCA* and PSPC data, with the SIS energy range being 0.4-10.0 keV in column 2 and 0.6-10.0 keV in column 3.  $N_H$  is applied to all components while  $N_{H,2}$  and  $N_{H,3}$  are applied only to the second Raymond-Smith and the power-law components, respectively.